SANDIA REPORT
SAND2011-6497
Unlimited Release
Printed September 2011

Experimental Investigation of the Richtmyer-Meshkov Instability

Christopher R. Weber

Prepared by
Sandia National Laboratories
Albuquerque, New Mexico 87185 and Livermore, California 94550

Sandia National Laboratories is a multi-program laboratory managed and operated by Sandia Corporation, a wholly owned subsidiary of Lockheed Martin Corporation, for the U.S. Department of Energy's National Nuclear Security Administration under contract DE-AC04-94AL85000.

Issued by Sandia National Laboratories, operated for the United States Department of Energy by Sandia Corporation.

Available to DOE and DOE contractors from
U.S. Department of Energy
Office of Scientific and Technical Information
P.O. Box 62
Oak Ridge, TN 37831

Telephone: (865) 576-8401
Facsimile: (865) 576-5728
E-Mail: reports@adonis.osti.gov
Online ordering: http://www.osti.gov/bridge

Available to the public from
U.S. Department of Commerce
National Technical Information Service
5285 Port Royal Rd.
Springfield, VA 22161

Telephone: (800) 553-6847
Facsimile: (703) 605-6900
E-Mail: orders@ntis.fedworld.gov
Online order: http://www.ntis.gov/help/ordermethods.asp?loc=7-4-0#online

SAND2011-6497
Unlimited Release
Printed September 2011

Experimental Investigation of the Richtmyer-Meshkov Instability

Christopher R. Weber
University of Wisconsin-Madison
1500 Engineering Drive
Madison, WI 53706

Abstract

The Richtmyer-Meshkov instability (RMI) is experimentally investigated using several different initial conditions and with a range of diagnostics. First, a broadband initial condition is created using a shear layer between helium+acetone and argon. The post-shocked turbulent mixing is investigated using planar laser induced fluorescence (PLIF). The signature of turbulent mixing is present in the appearance of an inertial range in the mole fraction energy spectrum and the isotropy of the late-time dissipation structures. The distribution of the mole fraction values does not appear to transition to a homogeneous mixture, and it is possible that this effect may be slow to develop for the RMI. Second, the influence of the RMI on the kinetic energy spectrum is investigated using particle image velocimetry (PIV). The influence of the perturbation is visible relatively far from the interface when compared to the energy spectrum of an initially flat interface. Closer to the perturbation, an increase in the energy spectrum with time is observed and is possibly due to a cascade of energy from the large length scales of the perturbation. Finally, the single mode perturbation growth rate is measured after reshock using a new high speed imaging technique. This technique produced highly time-resolved interface position measurements. Simultaneous measurements at the spike and bubble location are used to compute a perturbation growth rate history. The growth rates from several experiments are compared to a new reshock growth rate model.

Contents

Abstract 3
Contents 5
Figures 6
Acronyms 7
1.0 Introduction 9
2.0 Experimental Facility 10
3.0 Turbulent Mixing in the Richtmyer-Meshkov Instability 11
3.1 Background 11
3.2 Experimental Setup 12
3.3 Interface Characterization 13
3.4 Image Processing 15
3.5 Results and Discussion 16
Mixing Statistics 18
Dissipation Rate 19
Spectra 22
4.0 Influence of the Richtmyer-Meshkov Instability on the Kinetic Energy Spectrum 24
4.1 Background 24
4.2 Experimental Setup 25
4.3 Fluctuating Kinetic Energy Spectra 29
4.4 Simulation 33
4.5 Summary and Discussion 35
5.0 Richtmyer-Meshkov Instability on a Low Atwood Number Interface after Reshock 36
5.1 Background 36
5.2 Experimental Setup 36
5.3 Experimental Results 37
Model Comparison 39
5.4 Numerical Simulation 43
6.0 Summary and Conclusion 45
7.0 References 46
Distribution 49

Figures

Figure 1: Diagram of the initial condition setup. 12
Figure 2: Initial condition image and spectrum.. 13
Figure 3: Initial condition images in the x-y plane.. 14
Figure 4: Spectra in the x and y directions.. 15
Figure 5: Image correction. 16
Figure 6: Selected images from experimental sequence. 17
Figure 7: PDF of mole fraction at <X>=0.5 19
Figure 8: Log of the dissipation rate. 22
Figure 9: PDF of the dissipation rate. 21
Figure 10: PDF of the gradient angles.. 22
Figure 11: Light-gas mole fraction energy spectra 22
Figure 12: Dissipation spectra 23
Figure 13: Initial condition.. 25
Figure 14: Post-shocked interface and regions of interest. 26
Figure 15: PIV results.. 27
Figure 16: Particle lag after an impulsive acceleration. 28
Figure 17: Semi-log plot of fluctuating kinetic energy. 29
Figure 18: Kinetic energy spectrum at early time. 30
Figure 19: Kinetic energy spectrum at late time.. 31
Figure 20: Kinetic energy spectra for wave interface. 32
Figure 21: Kinetic energy spectra for flat interface.. 32
Figure 22: Analysis regions in simulation. 33
Figure 23: Kinetic energy spectra from simulation using full domain width. 34
Figure 24: Kinetic energy spectra from the simulation using the smaller region.. 34
Figure 25: Initial condition image and modal content.. 37
Figure 26: Planar images of the instability.. 38
Figure 27: Experimental x-t diagram 38
Figure 28: Amplitude vs. time after reshock 39
Figure 29: Diagram of a shock wave passing through a light-over-heavy sinusoidal interface 40
Figure 30: Experimental amplitude growth rate divided by the model growth rate.. 42
Figure 31: Simulation results 43

Acronyms

CCD	Charge Coupled Device
DFT	Discrete Fourier Transform
ICF	Inertial Confinement Fusion
PDF	Probability Density Function
PIV	Particle Image Velocimetry
PLIF	Planar Laser Induced Fluorescence
RMI	Richtmyer-Meshkov Instability
RTI	Rayleigh-Taylor Instability

Experimental Investigation of the Richtmyer-Meshkov Instability

1.0 Introduction

The Richtmyer-Meshkov instability (RMI) [1, 2] occurs when a shock wave passes through an interface separating a pair of gases. Any perturbation on that interface is unstable to the shock acceleration and will grow in amplitude. If the amplitude is much less than the wavelength, the growth is linear and given by the equation

$$\dot{\eta} = kA^{+}V_0\eta_0^{+}, \tag{1}$$

where k is the wavenumber, $A = (\rho_2 - \rho_1)/(\rho_2 + \rho_1)$ is the Atwood number, V_0 is the velocity of an unperturbed interface after acceleration by the shock wave, and η_0 is the initial amplitude. The superscript "+" denotes post-shocked quantities.

The mixing that results from the RMI becomes important during the compression of an inertial confinement fusion (ICF) fuel capsule [3], behind the shock wave of a supernova [4], and as a mechanism for mixing fuel in hypersonic engines [5]. In all of these applications, knowledge of how the instability develops over time and the role certain parameters play in the instability is of current interest. New insight is gained in this problem through developing models based on well-understood concepts, such as linear stability theory or buoyancy and drag, and comparing their modeling of the RMI to experimental and numerical data. Additionally, multiphysics codes used to simulate high-energy regimes, such as that during ICF or supernova explosion, need experimental data for validation. Experiments of the RMI provide useful test cases for the hydrodynamic component of these codes.

The current work explores three areas where experimental knowledge of the RMI is minimal. The mixing mechanisms inside a turbulent mixing layer are investigated using planar laser induced fluorescence (PLIF). The influence of the kinetic energy spectrum due to the RMI is analyzed through particle image velocimetry (PIV). Finally a new technique is introduced to measure the growth rate of a single mode interface after reshock.

2.0 Experimental Facility

The experiments are performed at the Wisconsin Shock Tube Laboratory [6]. The shock tube is a downward firing, 9.13 m vertical tube. The driver has a circular cross section with a 0.41 m radius and a 2.08 m length while the driven section has a square cross section with 0.25 m sides. A high-pressure boost tank is connected to the driver section by pneumatically-driven fast-opening valves to control the diaphragm rupture time. Piezoelectric pressure transducers mounted along the shock tube side walls are used to trigger the controlling electronics and to measure the shock wave speed.

Before the experiment begins, the driver is filled to 85%-90% of the diaphragm rupture pressure. The experiment is initiated by opening the fast-opening valve, filling the driver with high pressure gas from the boost tank, and rupturing the diaphragm. The long length of the shock tube ensures a planar shock wave by the time it reaches the interface. Between opening the valves and the shock wave arriving at the interface, approximately 400 ms has elapsed with a variability of about 50 ms.

3.0 Turbulent Mixing in the Richtmyer-Meshkov Instability

3.1 Background

Applications of the RMI have initial conditions that consist of a broadband spectrum of modes [7], but the bulk of experimental work has focused on single mode initial conditions. This is partially because generating a broadband initial condition in the lab is difficult to control. It requires either an unknown initial condition [8], a interface that is disturbed by membrane fragments [9], or laser-driven experiments with poor spatial resolution [10].

High spatial resolution and knowledge of the initial condition are required to explore the mixing dynamics between the two gases, where gradients in the mole fraction become important. To understand these dynamics, an equation describing the mixing rate can be derived starting with the continuity equation,

$$\frac{\partial \rho}{\partial t} + \nabla \cdot (\mathbf{u}\rho) = 0 . \tag{2}$$

We assume the fluid is variable density but incompressible, which is an adequate assumption after the shock has passed through the interface. If we nondimensionalize by reference values of density and velocity, we get a nonzero divergence of the velocity [11] :

$$\nabla \cdot \mathbf{u} = -\frac{1}{\mathrm{Re}\,\mathrm{Sc}} \nabla \cdot \left(\frac{1}{\rho} \nabla \rho \right), \tag{3}$$

where the $\mathrm{Re} = UL/\nu$ is the Reynolds number, $\mathrm{Sc} = \nu / D$ is the Schmidt number, and D is the mass diffusivity. Expanding the continuity equation and using Eq. (3) gives

$$\begin{aligned} \frac{\partial \rho}{\partial t} + \mathbf{u} \cdot \nabla \rho &= \frac{\rho}{\mathrm{Re}\,\mathrm{Sc}} \nabla \cdot \left(\frac{1}{\rho} \nabla \rho \right) \\ &= -\frac{1}{\mathrm{Re}\,\mathrm{Sc}} \frac{1}{\rho} (\nabla \rho \cdot \nabla \rho) + \frac{1}{\mathrm{Re}\,\mathrm{Sc}} \nabla^2 \rho \end{aligned} \tag{4}$$

Density can be replaced with the mole fraction, $X = (\rho - \rho_1)/(\rho_2 - \rho_1)$, giving

$$\left[\frac{\partial}{\partial t} + \mathbf{u} \cdot \nabla - \frac{1}{\mathrm{Re}\,\mathrm{Sc}} \nabla^2 \right] X = -\frac{1}{\mathrm{Re}\,\mathrm{Sc}} \frac{(\eta - 1)}{1 + (\eta - 1) X} (\nabla X \cdot \nabla X) \tag{5}$$

where eta is the density ratio. The right side of this equation is strictly negative and will act to reduce gradients in the mole fraction field, making the flow more homogeneous. To follow along the lines of scaling mixing investigations [12–14], this equation can be put in a form similar to the scalar 'energy' per unit mass, $\frac{1}{2}X^2$:

$$\left[\frac{\partial}{\partial t} + \mathbf{u} \cdot \nabla - \frac{1}{\mathrm{Re}\,\mathrm{Sc}} \nabla^2 \right] \tfrac{1}{2} X^2 = -\frac{1}{\mathrm{Re}\,\mathrm{Sc}} \left(2 - \frac{1}{1 + (\eta - 1) X} \right) (\nabla X \cdot \nabla X) . \tag{6}$$

This is the same as the equation arrived at when starting from the advection-diffusion equation for a conserved passive scalar, except for the factor on the right:

$$2 - \frac{1}{1 + (\eta - 1) X} = 2 - \frac{\rho_1}{\rho}, \tag{7}$$

which ranges from 1, where □=□$_1$, to a maximum of 2 if □$_2$>> □$_2$. If □$_1$=□$_2$, then we are simply tracking the mixing of a conserved passive scalar. The addition of variable density adds weight to dissipation in the higher density areas. In this work, to be consistent with similar work [15], the dissipation rate is referred to as $\chi = D\nabla X \cdot \nabla X$.

3.2 Experimental Setup

An interface of helium mixed with acetone vapor above pure argon is created 1 m above the end wall of the shock tube. The helium+acetone mixture is made by bubbling helium through two chambers of liquid acetone, the first being heated to 35 °C and the second at room temperature. The gas stream is then piped through chilled water so the acetone concentration is slightly below saturation and does not condense in the flow-metering equipment. The mixture is at a pressure of 50 psi to achieve a sufficient flow rate, resulting in an acetone vapor concentration of 5.3%. The helium+acetone mixture is split to the top of the shock tube and to the interface section. An initially flat interface is first set up by only flowing helium+acetone into the top of the shock tube and argon into the bottom. Excess gas is evacuated through a pair of vacuum pumps connected to slots in the shock tube wall at the interface location.

To create a perturbed interface, the helium+acetone mixture and pure argon are injected through separate slots into the shock tube. The configuration, shown in Figure 1, was experimentally determined to provide the best initial condition in terms of scale and repeatability. Introducing argon above the helium+acetone mixture acts to keep the mixing layer horizontal. Perturbations appear due to the interaction between the two streams and from the shear between this mixed layer and the pure argon. In addition to the gas injected at the shear layer, gas is also injected at both ends of the shock tube. This creates a continual flow towards the interface, ensuring that all of the mixed gas is removed and the mixing layer is steady in time.

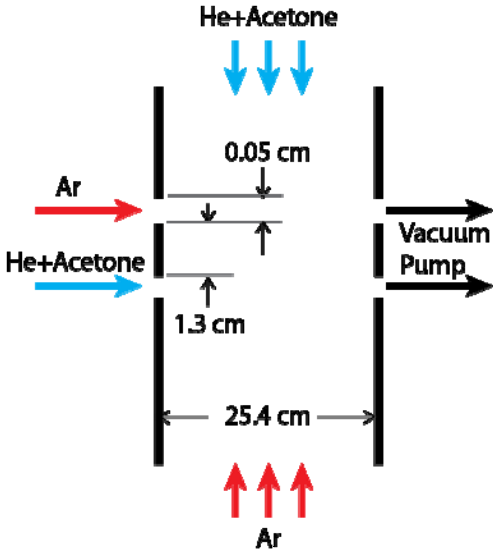

Figure 1: Diagram of the initial condition setup.

Two excimer lasers (Lambda Physik LPX 210i, 308 nm, 470 mJ) are used for planar imaging. The laser beams are combined below the shock tube using a 50-50 beamsplitter and then spread

into a sheet with a combination of spherical and cylindrical lenses. A single laser is used for both the initial condition imaging and a post-shock image, while the other is used for the second post-shock image. Ten pre-shock images are recorded prior to the arrival of the M=1.56 shock wave to obtain a statistical description of the initial condition. To allow the laser to recharge and account for variability in experimental timing, the last initial condition occurs around 150 ms prior to the shock arriving at the interface. The laser is fired again 0.88 ms after shock arrival to capture the post-shock interface after it has traveled 26.5 cm. The second laser fires 2.1 ms after shock arrival, capturing the final post-shock image where the interface has traveled 67.3 cm. Twenty experiments were performed with these settings to obtain an ensemble average. Alternately, five early time experiments were performed where the first post-shock image is still in the frame of the first camera. The images are all recorded using 3 thermoelectrically cooled Andor CCD cameras.

3.3 Interface Characterization

Figure 2(a) shows a sample of the initial condition, corrected so intensity corresponds to relative acetone concentration or light-gas mole fraction, X. In the image, the gases are injected from the left near z = 0 cm. The pure argon stream is visible above the helium+acetone mixture. After about 3 cm, the two streams of gas begin mixing and the individual streams are no longer apparent. Perturbations develop on the lower edge of this mixing region due to the velocity difference of the mixture stream and the ambient argon. An additional contour is visible rising from the injection location and running horizontally near z = 4 cm. This appears to be the boundary between the mixed gas and pure helium+acetone entering from the top of the shock tube. This top contour is diffuse, without perturbations developing on it. Between this top contour and the bottom shear surface, the average mole fraction is around 0.75. The red dashed lines in Figure 2(a) mark the location where the average mole fraction in the x direction is 0.25, 0.5, and 0.75.

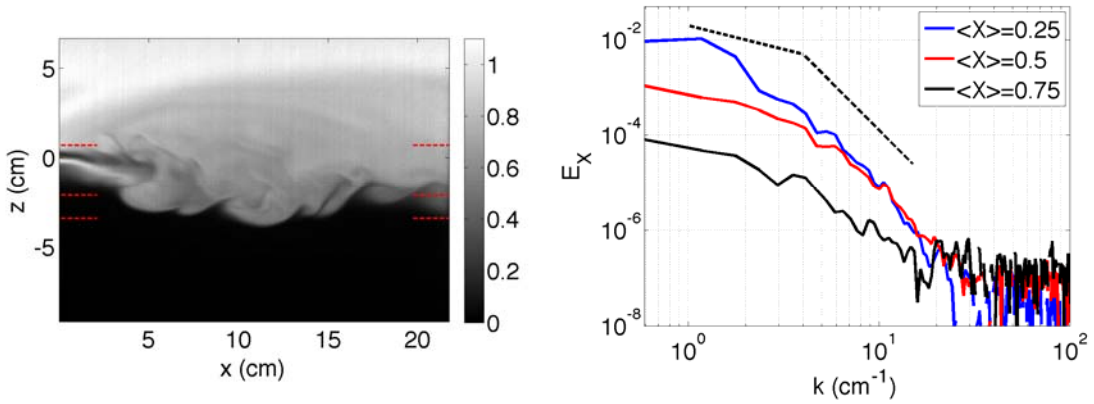

Figure 2: Initial condition image and spectrum. (a) A sample initial condition image, processed so intensity corresponds to relative acetone concentration,. The red dashed lines correspond to locations where the average mole fraction in the x direction is 0.25, 0.5, and 0.75. (b) The mole fraction energy spectra from locations denoted in (a), averaged over 40 images.

Figure 2(b) shows the energy spectrum of the mole fraction at locations where $\langle X \rangle$ = 0.25, 0.5, and 0.75. These spectra are averages from 40 images. The dashed lines represent a k^{-1} and k^{-4} spectra, which roughly match the spectrum at $\langle X \rangle$ = 0.5.

These experiments are investigating a 2-dimensional slice in the *x*-*z* plane, so it is necessary to determine how representative this slice is of the whole experiment. To answer this, the initial condition was imaged in the *x*-*y* plane by placing the laser in this plane and positioning the camera below the shock tube, looking in the *z* direction. These images allow us to determine if the perturbations are 2 or 3 dimensional and if the interface is nearly isotropic in the *x* and *y* directions.

Images of the initial condition in the *x*-*y* plane are shown in Figure 3 at 6 *z*-locations, ranging from *z*=2.54 cm to *z*=-2.54 cm. Gas is injected from the left in these images. At the top of the mixing layer, Figure 3(a), there appears to be more mixing features near the edges in the *y*-direction than in the center. At the next lower plane, the variation in the *y*-direction is nearly gone. The gradients appear to be sharper towards the left of the image, which is to be expected since diffusion and mixing have more time to smooth out gradients by the time the gases reach the right side. The plane shown in Figure 3(c) is similar to the one above it, with some variation in the *y*-direction near the left of the image. The bottom two locations seem to be primarily composed of ambient argon, with mixed gas entering the plane in the center of the image.

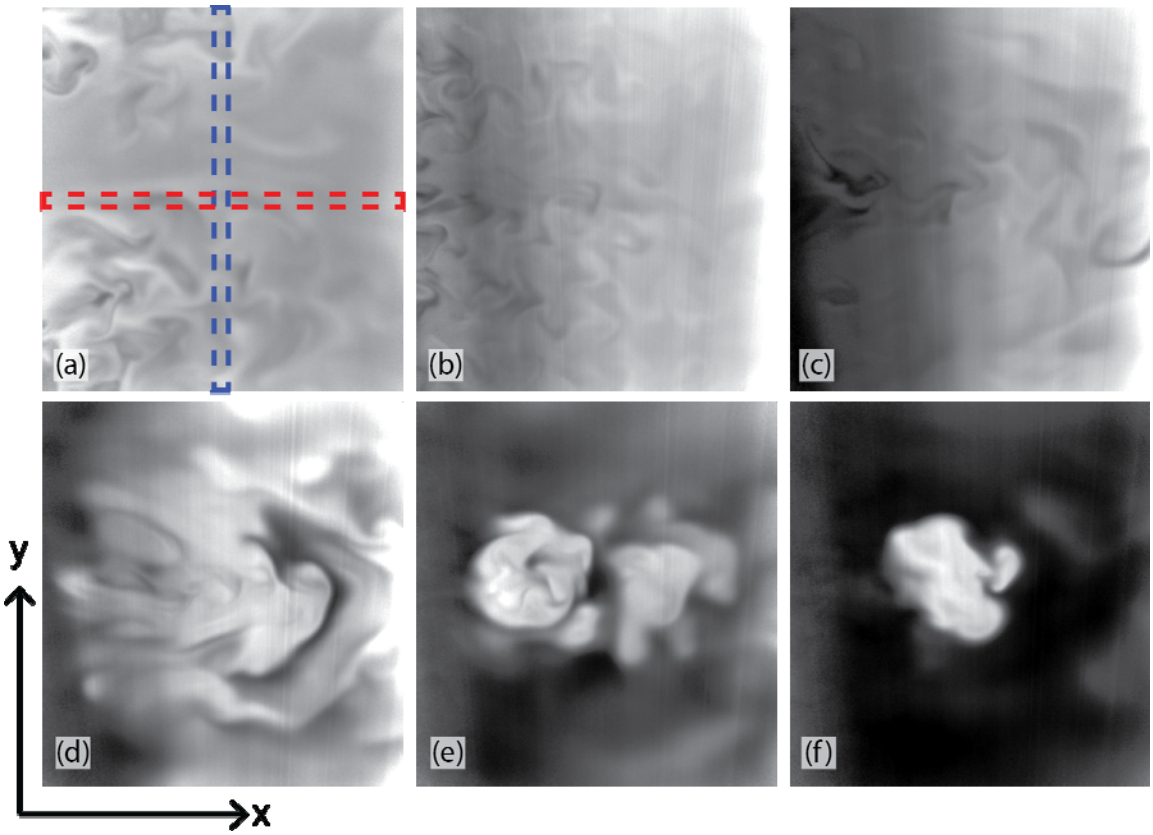

Figure 3: Initial condition images in the *x*-*y* plane. Image planes are located at (a) *z* = 2.54cm, (b) *z* = 1.27 cm, (c) *z* = 0, (d) *z* = -1.27, (e) *z* = -1.91, and (f) *z* = -2.54.

Spectra are shown in Figure 4 comparing the spectrum at the center of the image in the *x* direction (k_x spectrum, region overlaid in red in Figure 3(a)) with the k_y spectrum in the *y* direction (region overlaid in blue). The spectra are computed using 11 rows or columns of data

from each image and from 40 images at each plane. In the image at the highest location, Figure 3(a), we saw fewer features in the center of the *y*-direction than near the edges; the spectra also show this difference, Figure 4(a), with the k_x spectrum being weaker than the k_y spectrum at moderate wavenumbers. The next two locations, Figure 4(b,c), have similar spectra at moderate wavenumbers, but at low wavenumbers the k_x spectrum is larger. The low wavenumber effect is visible in the images, as the left of the image appears darker; it is possible that this is due to a nonuniform laser beam or a problem in the images correction step. The last three locations, Figure 4(d-f), show very similar spectra for nearly all wavenumbers. It appears that, for a large portion of the initial interface, the perturbation features are isotropic in the *x* and *y* directions.

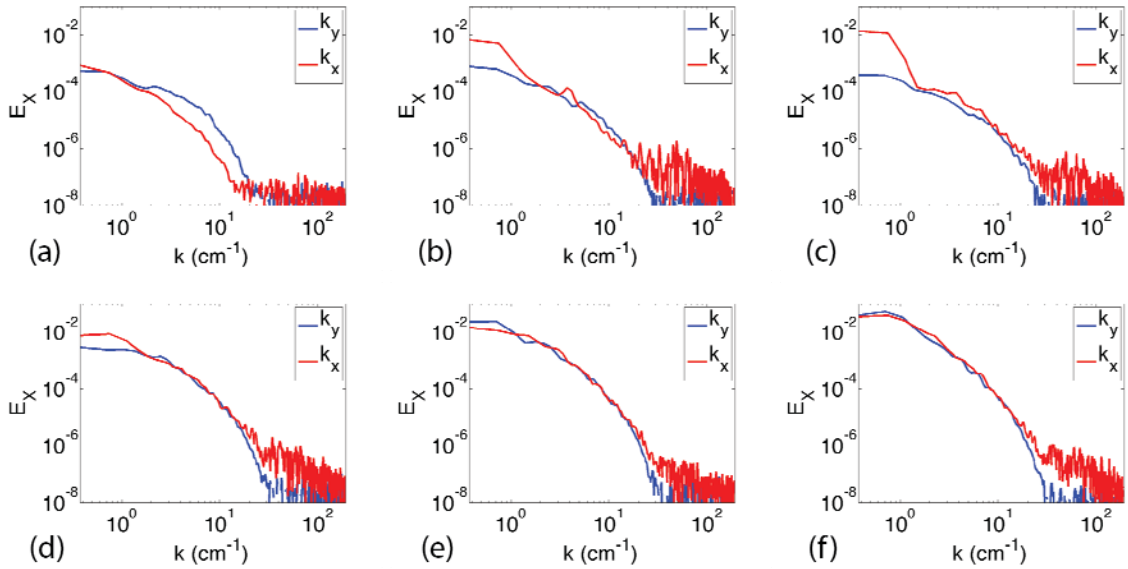

Figure 4: Spectra in the *x* and *y* directions. (a-f) correspond to the locations in Figure 3(a-f) respectively. The locations where the spectra were computed are shown in Figure 3(a).

3.4 Image Processing

To translate the raw PLIF images into relative acetone concentration, the images are corrected for non-uniform laser profile, laser sheet divergence, and Beer's law attenuation. An uncorrected PLIF image is shown in Figure 5(a). The general procedure is to transform the image into an *r*-□ coordinate system aligned with the laser beam and correcting for the signal decrease from laser sheet divergence. Then a region in the top of the image is selected where it is assumed a uniform concentration exists. The exponential coefficient of the signal as a function of *r* is determined from this region, corresponding to the acetone absorption cross-section, □. The normalized acetone concentration can then be computed [16]:

$$X(r,\theta) = \frac{i(r,\theta)}{i_0(\theta) - \sigma \int_R^r i(r',\theta)\,dr} \tag{8}$$

where $i(r,\square)$ is intensity of a given pixel and $i_0(\square)$ is the pixel intensity at the top of the image. The image is then mapped back into the *x*-*z* coordinate system.

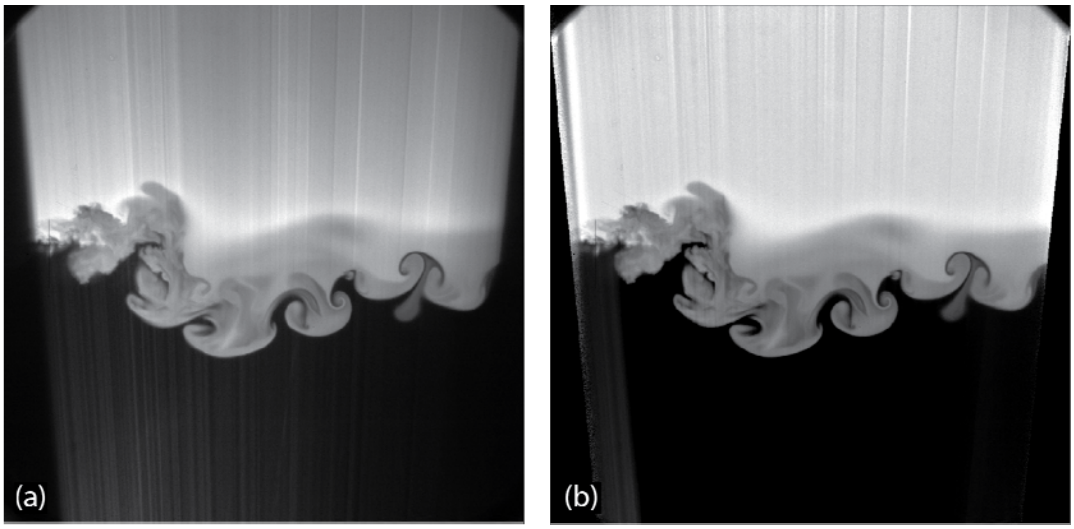

Figure 5: Image correction. (a) Uncorrected image and (b) corrected image with intensity proportional to acetone concentration.

Some fine-scale features in the top of the laser sheet are not due to the aforementioned effects. As the laser sheet passes through the interface, index of refraction gradients will steer some rays in different directions causing them to not map correctly into the *r*-□ coordinate system. Furthermore, the location where they originate can be anywhere within the mixing layer, so their inclusion in Eq. (8) could introduce unwanted effects into the corrected image. Because of this, high frequency components in the reference intensity i_0 were removed.

The two post-shocked image cameras are much slower than the duration of the experiment and are exposed for the entire duration. Because of this, both cameras capture two laser pulses. There is no acetone in the frame during the extra laser pulse for the final post-shock exposure, so this only adds to the background illumination and is easily corrected. For first post-shocked image, the extra laser pulse illuminates the region far upstream from the interface where the concentration is uniform. This additional signal is roughly an order of magnitude weaker than the signal from the desired laser pulse because the laser has attenuated significantly before entering the frame, but it still should be corrected for. The region below the interface in the first post-shocked image is assumed to be the constant concentration illumination from the extra pulse. The beam profile is detected in this region along with its spread and attenuation. This profile is then extrapolated to the full frame and subtracted from the original image. Following this, the above procedure is followed to determine relative concentration. Figure 5(b) shows the corrected image with intensity proportional to acetone concentration.

3.5 Results and Discussion

Figure 6 shows a sample of corrected images from the experimental campaign. The laser sheet in the late-time location, near the end wall of the shock tube, is narrower than locations further from the end wall, so all images are cropped to the dimensions of the laser sheet in the late-time images. The first row in Figure 6 shows three initial condition images. The second, third and fourth rows of images are at post-shock times of 0.14 ms, 0.88 ms, and 2.10 ms respectively. Images in the same column in rows three and four are from the same experiment.

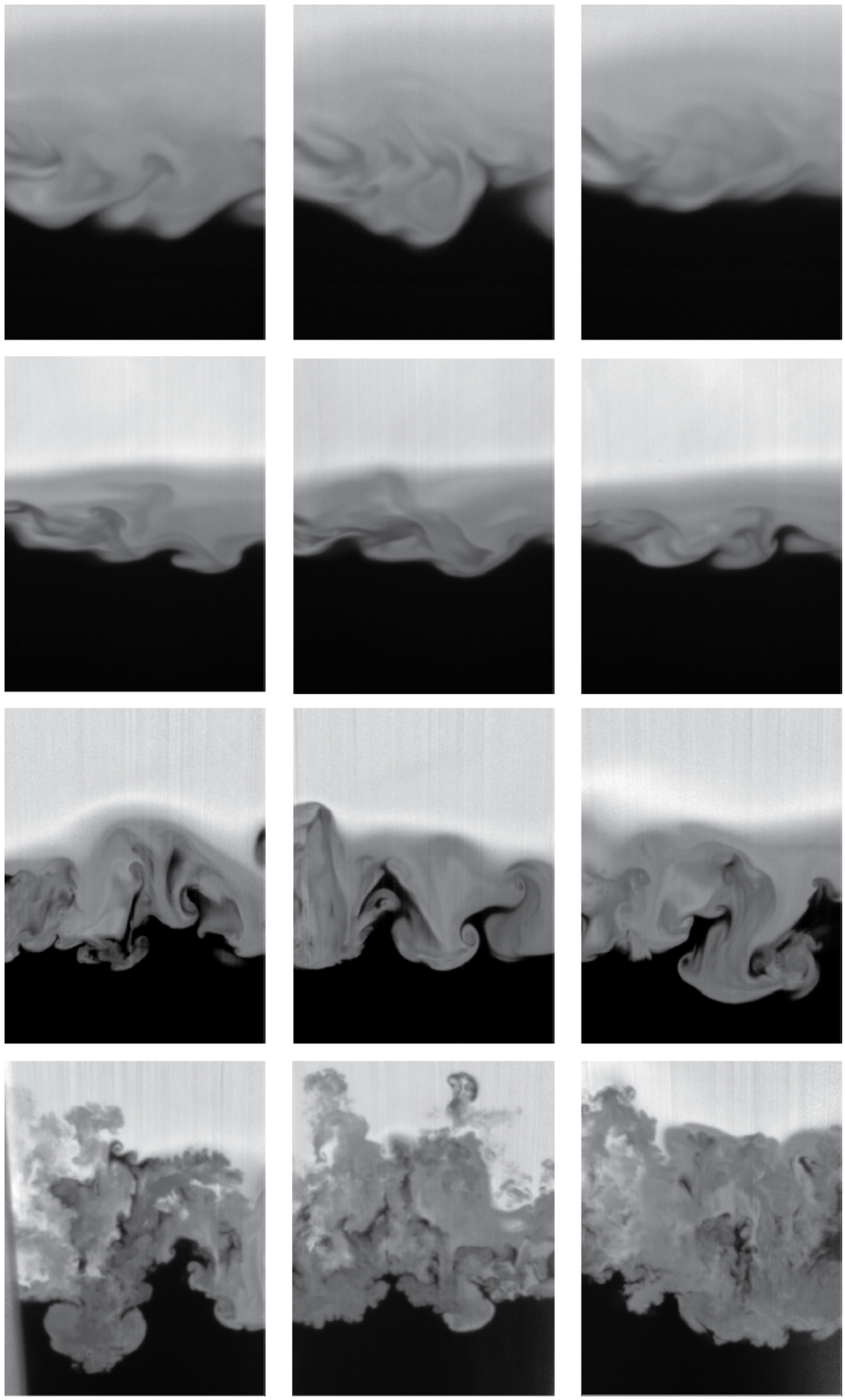

Figure 6: Selected images from experimental sequence. First row: initial condition images. Second row: 0.14 ms after shock-interaction. Third row: 0.88 ms after shock interaction. Fourth row: 2.10 ms after shock interaction. The width of each image is 8.2 cm.

The images show that the large-scale extent of the mixing layer is growing, while the fluid within the layer is becoming more mixed and turbulent. The earliest post-shock images seem to have similar features as the initial conditions, but the gradients are somewhat sharper, likely due to the compression from the shock wave. The post shock images at 0.88 ms each appear to be dominated by several argon spikes penetrating into the lighter gas. The interface dividing these spikes from the mixed fluid appears relatively smooth, without significant secondary Kelvin-Helmholtz instabilities. By 2.10 ms the smoothness along the interface is gone and many small-scale features are present along most contours levels.

Mixing Statistics

The large-scale length of the interface is measured by averaging across the width of the image to obtain an average mole fraction profile, $\langle X \rangle(z)$. The distance between the $\langle X \rangle$=0.05 and $\langle X \rangle$=0.95 values is used as a measure of mixing layer thickness. An alternate mixing layer thickness, called mixing product thickness h [11], is defined as

$$X_p(X) = \begin{cases} 2X & \text{for } X \le 0.5 \\ 2(1-X) & \text{for } X > 0.5 \end{cases}, \tag{9}$$

$$h = \int_{-\infty}^{\infty} X_p\left(\langle X \rangle\right) dz. \tag{10}$$

The three post-shock mixing thickness values are used to estimate the thickness growth rate, giving 24.5 m/s for the $\langle X \rangle$=0.05-0.95 definition and 17.0 m/s for the integral definition. From this, the Reynolds number is calculated, $\mathrm{Re} = h\dot{h}/\nu$. Table 1 shows the values for mixing thickness and Reynolds number. The Reynolds number is above the proposed threshold for a transition to turbulent mixing, $2\text{x}10^4$ [17].

Table 1: Large-scale thickness and Reynolds number

	Time (ms)	$h_{5\text{-}95}$ (cm)	h_p (cm)	$\mathrm{Re}_{5\text{-}95}$	Re_p
IC	0	6.0±0.5	4.0±0.4		
PS1	0.137	3.4±0.2	2.1±0.4	5.55E+04	2.37E+04
PS2	0.881	5.5±0.4	3.0±0.5	8.95E+04	3.36E+04
PS3	2.104	8.3±1.0	5.4±0.9	1.35E+05	6.11E+04

The above definition of mixing thickness does not differentiate between mixed gas and unmixed but interpenetrating gas. This difference can be expressed in the following ratio [11]:

$$\Xi = \frac{\int \langle X_m(X) \rangle dz}{\int X_m\left(\langle X \rangle\right) dz}, \tag{11}$$

where the denominator is our previous definition of mixing product thickness and the numerator averages *after* converting the mole fraction field into a mix fraction field. This ratio is very high for the entire experiment, starting at 0.98 for both the initial condition and the earliest post shock time. For the middle and late post-shock times, the ratio is 0.92 and 0.87 respectively. This trend is comparable to that of a similar type of flow [18], which finds the mixing fraction start near 1, drop for a short period, and then increase after the turbulent mixing transition to near 0.8. While this ratio is decreasing, the net amount of mixed gas, determined by the numerator, is increasing, going from 2.1 cm at the first post-shock time to 4.7 cm by the third post-shock time.

The amount of mixing at the <*X*>=0.5 location is shown in Figure 7. Initially the mole fraction is well mixed at this location, with a peak in the distribution around *X*=0.5. Later in time, the distribution broadens, spanning over a wider range of mole fraction values. After the transition to turbulent mixing, it has been observed that the distribution becomes more homogeneous with a narrower distribution peak [17–20]. In the current experiments, the growth of large-scale perturbations introduce unmixed gas into the mixing region, initially reducing the amount of mixed gas. Viscosity and diffusion will reduce these large-scale perturbations into mixed fluid, which qualitatively appears to be occurring by the latest time images. Experimental measurement at later times than the current ones, which are not possible with the current experimental setup, may see the mole fraction PDF return to a narrow peak.

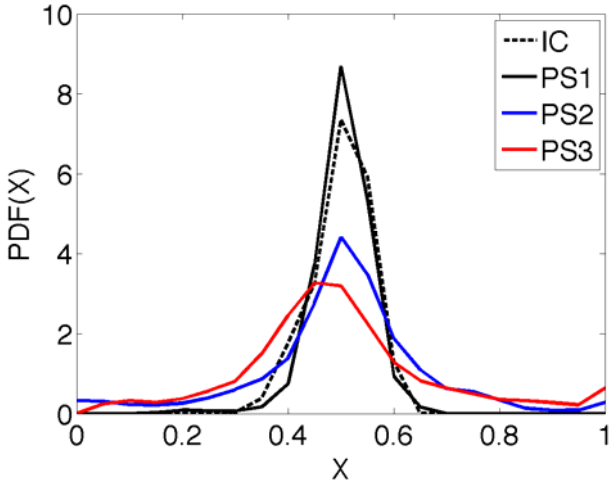

Figure 7: PDF of mole fraction at <X>=0.5

Dissipation Rate

The dissipation rate, $\chi = D\nabla\chi \cdot \nabla\chi$, is an important factor governing mixing: it provides insight into the rate at which mixing is occurring and the spatial properties of the mixing structures. To compute dissipation, the images are filtered through a 5x5 median filter and the gradient magnitude is calculated using an 8-point stencil [12]. Figure 8 shows the log of the dissipation rate from the images in Figure 6. The earlier two sets of images show long features stretching across the width of the image. At the time of the second post shock image, the structures are becoming more vertical as the heavy spikes protrude into the mixing layer. By the latest time, the mixing structures appear very chaotic without an obvious preferred direction. Vertical lines are present in the images above and sometimes below the interface. These are artifacts from distortions in the laser sheet that were not removed in the image processing step. To avoid counting these artifacts and limit the effect noise has on the statistics, a mask is applied to the images, keeping information only in the region 0.1<*X*<0.9. The masked image is used to calculate the net dissipation and PDFs from the dissipation data. The net dissipation rate for the 4 times are 5.8, 9.4, 32.2, and 53.0 cm^2/s.

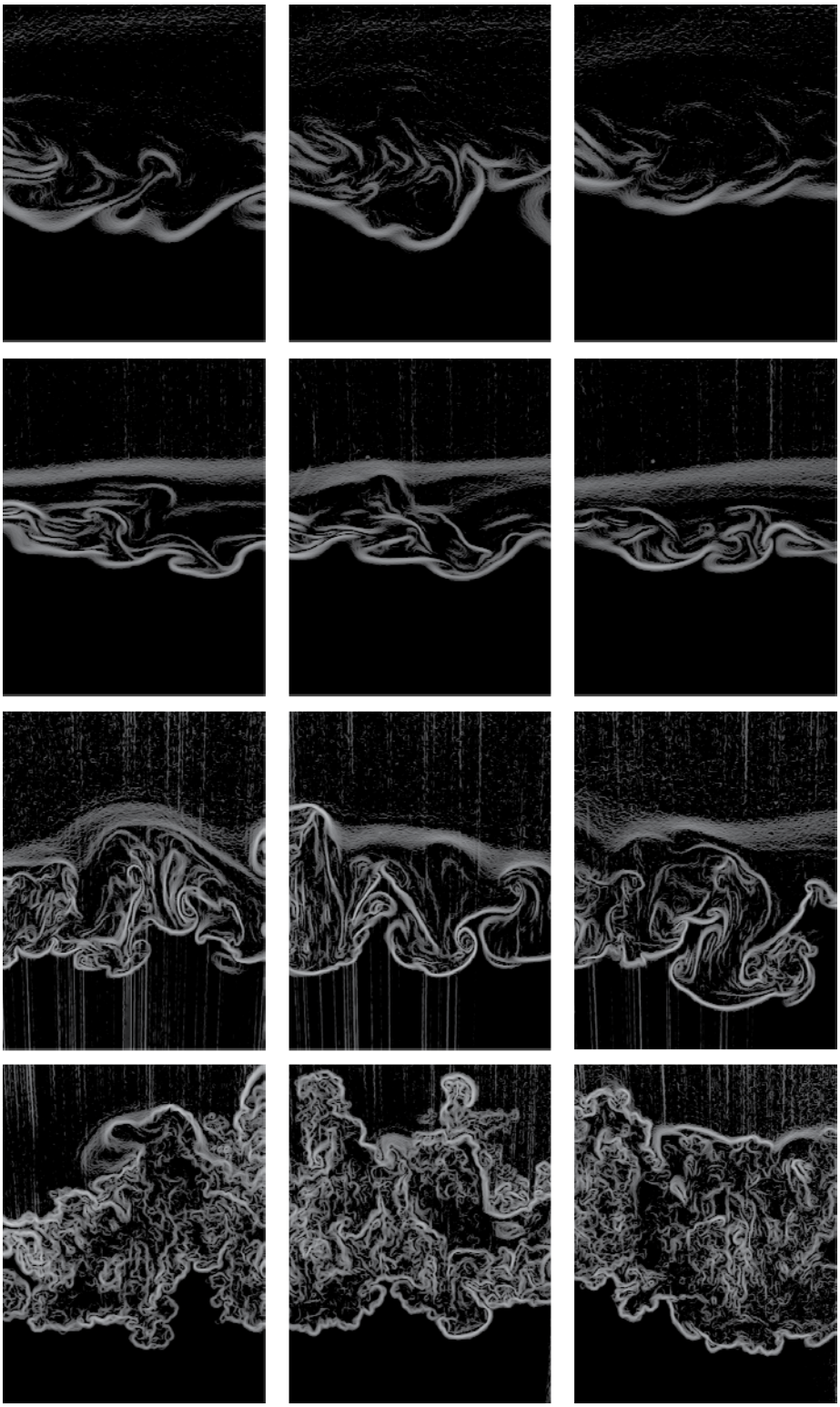

Figure 8: Log of the dissipation rate. Image time and location are the same as in Figure 6.

Figure 9 shows the PDF of the dissipation rate. We find an increase in magnitude to higher dissipation rates after the shock compresses the interface. The difference between the three post-shock times is not large, but the trend appears to be that the dissipation magnitude increases as time increases. The dissipation can be estimated from a scaling argument [14]:

$$\chi \sim 2DX_m^2 / \lambda_\beta^2, \tag{12}$$

where X_m is an average mole fraction and λ_β is the Batchelor length scale. This scale can be related to Reynolds number and the integral length scale [21]:

$$\lambda_\beta \sim \delta \mathrm{Re}^{-3/4} \mathrm{Sc}^{-1/2}. \tag{13}$$

In this flow, Sc~1 and $\mathrm{Re} \propto \delta$, so the Batchelor length scale should increase with time, while the estimate for dissipation should decrease. This is not what we observe from Figure 9, so it is likely that this scaling argument is insufficient and there is additional physics going on.

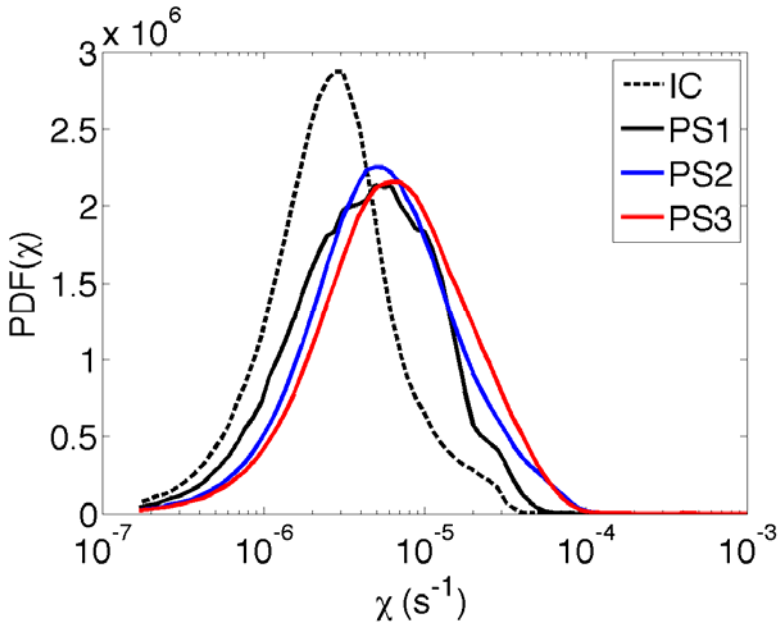

Figure 9: PDF of the dissipation rate for the initial condition and three post-shocked images.

The two components of the gradient of the light-gas mole fraction can be used to calculate the angle of the gradient. Initially we expect the main gradient to be in the vertical direction (90°). This is observable from the dissipation fields, where at early times the structures are mainly horizontal, signaling a gradient in the vertical direction. Figure 10 shows the PDFs of the gradient angles, where □ is measured counter-clockwise from the right direction in the images. Regions where the local dissipation was less than $5\text{x}10^{-7}$ s^{-1} were ignored. As expected, we see a large peak in the 90° direction. This peak increases after the shock interaction, where the shock wave compresses the interface in the streamwise direction, magnifying the gradients in that direction. In the later time experiments, this peak has reduced significantly. By the final image time, the gradient angle has only a slight preference for 90°, signifying that the mixing region has become nearly isotropic by this time.

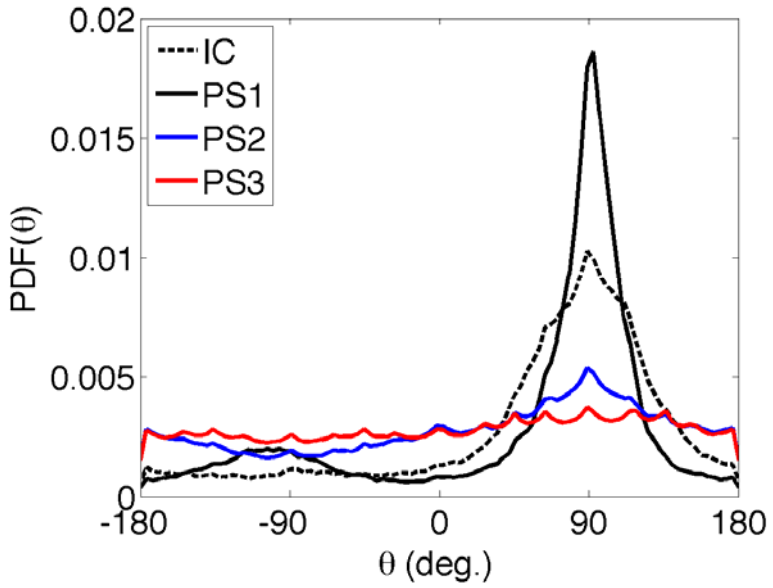

Figure 10: PDF of the gradient angles. The angle □ is measured counter-clockwise from the x axis.

Spectra

Power spectra are computed from the mole fraction fields at the <*X*>=0.5 location. Five rows on either side of the row nearest to <*X*>=0.5 are used to produce an average spectrum from each experiment. The spectrum from each row is interlaced with the neighboring row to reduce the effect of noise at high wavenumbers [22]. The average spectra from the 4 times are shown in Figure 11 with compensated spectra shown in Figure 11(b).

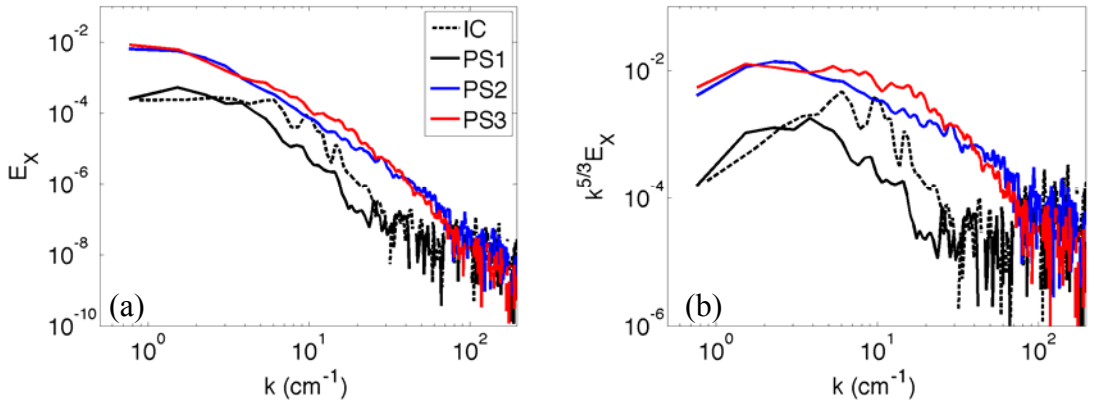

Figure 11: (a) Light-gas mole fraction energy spectra and (b) compensated spectra at <*X*>=0.5.

It is possible that an inertial range is developing in the late time spectrum between k=1.5 cm^{-1} and 8 cm^{-1}, as this region is nearly flat in the compensated spectrum of Figure 11(b). The dissipation spectra, $D=k^2E$, are shown in Figure 12. The Batchelor length scale can be estimated from the dissipation spectrum as the scale where the spectrum is 2% of the maximum [23]. Figure 12(b) is normalized to the maximum dissipation and a dashed line is showing the 2% level. The 2% level for the latest time experiments can be discerned, showing scale of 950 μm.

The spectrum of the earlier time experiments in Figure 12(b) becomes noisy at high wavenumbers near the 2% level, but it appears that the 2% scale would have been smaller than the later time scale, possibly around 730 μm. An increase in the Batchelor length scale with time is what we anticipated earlier from the scaling argument, $\lambda_\beta \sim \delta \mathrm{Re}^{-3/4}\,\mathrm{Sc}^{-1/2}$.

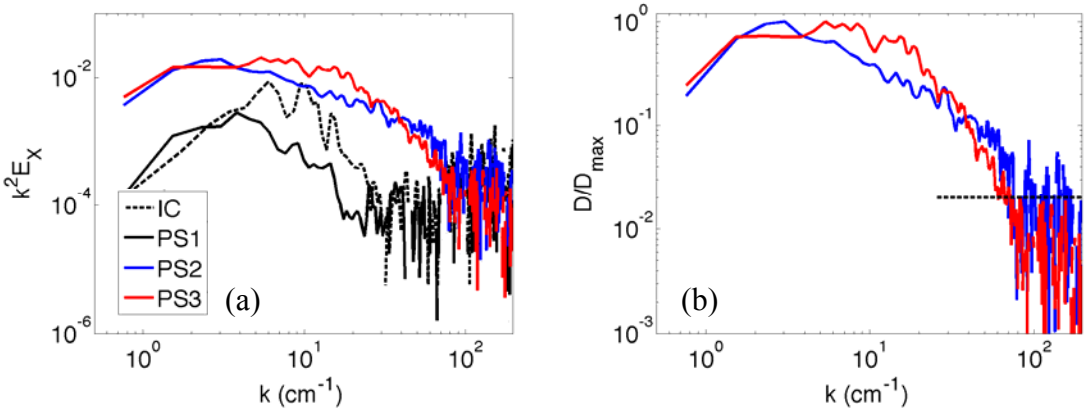

Figure 12: (a) Dissipation spectra and (b) normalized dissipation spectra with a dashed line representing the 2% level.

4.0 Influence of the Richtmyer-Meshkov Instability on the Kinetic Energy Spectrum

4.1 Background

RMI studies typically investigate the growth of the perturbation (for examples, see the review article by Bouillette [24]). Some effort has been made to study the turbulence that results from this perturbation growth. Laser doppler anemometry measurements have characterized the fluctuations inside the turbulent mixing zone, where dissipation and diffusion reduce the magnitude of the fluctuations but expand the spatial extent of this zone [25]. The mixing within a shocked gas-curtain showed that a late time transition to Kolmogorov scaling occurs [24,25]. The energy transfer within the Rayleigh-Taylor instability (RTI) was studied through direct numerical simulations [28], showing that energy is initially concentrated in scales corresponding to the dominant wavelength and spreads out to larger wavenumbers as vortex stretching and bending transfer energy to smaller scales.

A description of the energy scales in the RMI and how they vary in space and time is important to applications in inertial confinement fusion (ICF) and shock-induced mixing from supernova explosions. Simulations in these areas often use subgrid-scale models [27,28] to approximate the energy transfer to and from unresolved scales. These models rely on coefficients that need to be set to provide the best description of the underlying physics. An additional consideration, particularly in ICF, is the far-field effect of the instability. If the presence of a perturbation on the interface is felt far from the interface, it can have an influence on fusion ignition and burn wave propagation. This influence begins with the distorted transmitted shock wave converging to the capsule center.

When the shock wave passes from a light gas to a heavy gas, a reflected shock wave will propagate away from the interface through the light gas. This reflected shock wave initially takes on the distorted shape of the perturbed interface and, as it returns to planar, will leave a wake behind. This occurs because the concave portion of the distorted shock wave will converge slightly and strengthen. With the two refracted (transmitted and reflected) shock waves, the effect of the interface is felt far from the interface.

The interaction of the shock wave with the gas far from the interface can be described as being similar to the shock-turbulence interaction, where a shock wave passing through a turbulent field will amplify any existing turbulence in the flow [31]. In RMI experiments, any background turbulence present in the shock tube will also be amplified. In addition, the shock will interact differently with the longitudinal and transverse components, leaving behind an anisotropic turbulent field. After the interaction, without any additional production of turbulence, the turbulence will return to isotropic and decay through dissipation [23].

Additional production of turbulence, however, can be found near the interface of the RMI. A turbulent viscosity model [23] has the production term

$$P = \nu_T \frac{dU_1}{dx_2}. \tag{14}$$

The velocity gradients from the interfacial perturbation growth act as a source of turbulence that transfers to smaller length scales. The fluctuating kinetic energy spectrum initially contains energy at the large scales approximately equal to the wavelength of the perturbation. After some time, the spectrum will have filled out to the inertial sub-range, and then to the dissipation range. Cook and Zhou [28] described the energy spectrum in the RTI and showed that the dominant wavelength initially had the bulk of the kinetic energy, but as the instability developed the spectrum filled out to larger (due to bubble merger) and smaller scales. The main difference between the energy in the RTI and the RMI is that the former is continuously forced by the sustained acceleration field while the latter only has the energy left behind by the shock wave.

The perturbation growth and the interaction of the distorted shock wave with the surrounding gas leads to several turbulence mechanisms operating at different scales, locations, and times. The work discussed here analyzes the energy spectra at two times and at two locations with respect to the interface. The location further from the interface is considered similar to that of the shock-turbulence interaction, where dissipation and return to isotropy are the two processes that can be expected to occur. The turbulence at the location near the interface is expected to experience the additional production mechanism of the RMI perturbation growth.

4.2 Experimental Setup

A N_2-SF_6 interface is created by flowing N_2 from the top of the shock tube and SF_6 from the bottom. Slots, located 1 m from the bottom of the shock tube, allow a stagnation plane to form and excess gas to be removed with the aid of a vacuum pump. The slots are centered in a pair of 5.08×25.4 cm^2 rectangular pistons that are embedded in the wall of the shock tube wall. After the gases have flowed for a sufficient time to ensure purity, the pistons are oscillated at 3.27 Hz for 10 revolutions to create a 2-dimensional standing wave with an initial amplitude of 0.38 cm and a wavelength of 9.1 cm. An example of this initial condition is shown in Figure 13. The Atwood number of the interface is 0.68 initially and 0.77 after being compressed by the shock wave.

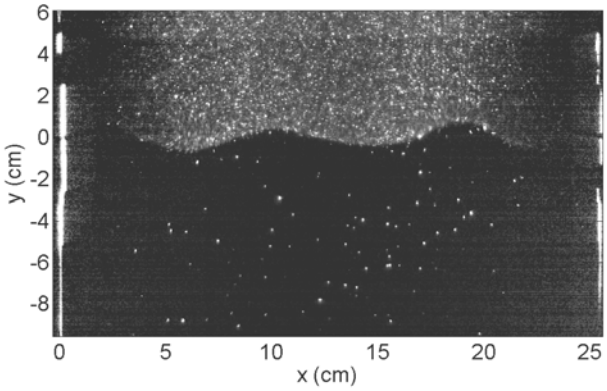

Figure 13: Initial condition. The N_2-SF_6 interface with the waveform initial condition is shown just prior to being accelerated by a shock wave. The N_2 is seeded with Al_2O_3 particles.

Prior to the experiment, the driver section is filled to 90% of the diaphragm rupture pressure. Excess pressure is then released into the driver using fast-opening valves that are timed in relation to the standing wave, rupturing the diaphragm and launching a shock wave towards the

interface. The shock wave has an incident Mach number of M=2.05 and the post-shocked interface velocity is 298 m/s.

Flow visualization is performed by seeding the N_2 with Al_2O_3 particles using a TSI fluidized bed (model 3400). Particles are mixed with the flow for approximately a minute prior to the experiment, allowing for a uniform particle distribution to be observed. Planar images are obtained using two lasers and three cameras. The initial condition is illuminated using a continuous Ar^+ laser of approximately 1W in power and spread into a sheet with a cylindrical lens. A high speed camera, IDT model XS4, is set up at the location of the stagnation plan to record the standing wave being created and determine the final interface shape before the shock reaches the interface. The post-shocked interface is recorded using two cameras and a dual-cavity Nd-YAG laser. The two pulses from the Nd-Yag laser are spaced 14 μs apart and have a pulse duration of ~10 ns. A LaVision Flowmaster 2 camera is focused onto a 2.2 cm x 2.8 cm region and records two images corresponding to each of the Nd-YAG pulses. A thermoelectrically cooled Andor CCD camera is mounted at an angle to the image plane to accommodate the LaVision camera, and provides a full-field view of the interface. The slow shutter on this camera requires that both Nd-YAG pulses are captured on a single image. Both cameras have a 532 nm laser line filter to allow only the light from the Nd-YAG laser.

Images obtained from two experiments are shown in Figure 14; each image was taken with the full-field camera and the rectangular boxes show the regions that the zoomed-in camera is focused on. The obstruction in the right half of the image is the LaVision camera. These images are taken at 0.3 ms and 1.0 ms after the shock wave accelerates the interface and the locations are 5 cm and 9 cm away from the interface at both times.

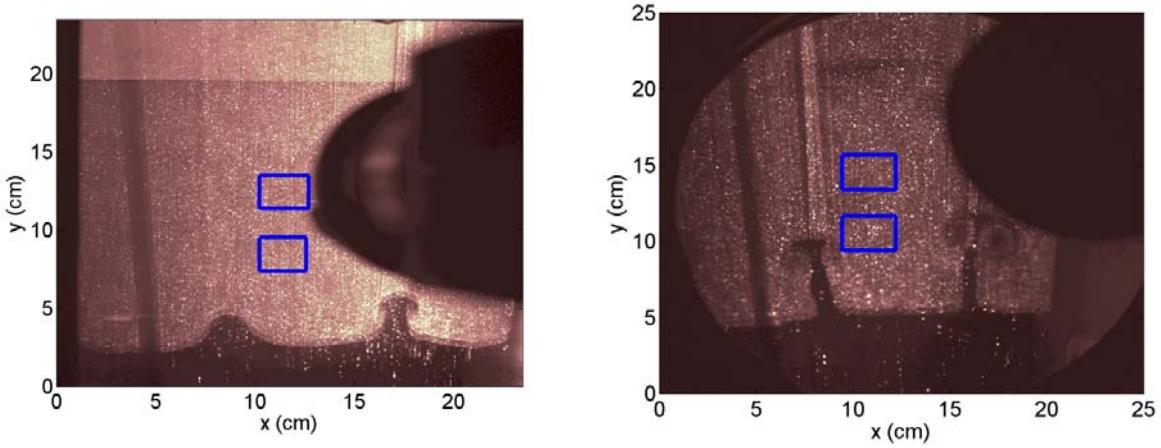

Figure 14: Post-shocked interface and regions of interest. These images are taken with the full-field camera at 0.3 ms and 1.0 ms showing the post-shocked interface with an initial waveform perturbation. The blue boxes show the regions that the PIV camera (black obstruction in the right half of the image) is focused on.

The pair of zoomed-in images is analyzed using particle image velocimetry (PIV) to obtain a velocity field. The mean flow has displaced 200 pixels between the two images, allowing small differences in the velocity field to be measured. The first step in the PIV analysis is to remove the background by subtracting a median filtered image from the original image. The background subtraction helps remove a zero-displacement bias of the cross-correlation procedure. The two

images are shifted by the estimated mean displacement and a cross-correlation analysis is applied to 64x64 pixel regions across the image to obtain the displacement field. The sub-pixel displacement is determined by assuming the cross-correlation matrix has a Gaussian shape and interpolating to find its peak location [32]. The displacement field is then filtered to remove spurious vectors and smoothed. The two images are then deformed using this displacement field and a bilinear interpolation algorithm. The first image is deformed by half the displacement field and the second is deformed in the opposite direction by half the displacement field, ideally resulting in two images with identical particle locations. A cross-correlation analysis is then applied to the deformed image. This process of image deformation and cross-correlation is iterated, without the smoothing step, until the deformed images have a negligibly small displacement field. This iteration occurred four times with a decreasing window size and increasing overlap, reaching a final size of 32x32 pixels with 50% overlap. This iterative image deformation method has been shown to improve the precision of sub-pixel displacement measurements by an order of magnitude over cross-correlation methods without image deformation [31,32].

An example of a velocity field from PIV is shown in Figure 15(a) from a late time image far from the interface which corresponds to the upper rectangular box in Figure 14 (b). The mean velocity of 298.2 m/s is removed, showing the fluctuating field. A reference vector of 5 m/s is shown in the upper right of the image and Figure 15(b) shows the magnitude of the velocity. The spatial resolution of the velocity field is 335 μm. The turbulent intensity, defined as

$$I = \frac{\sqrt{\langle u^2 \rangle}}{U}, \tag{15}$$

averaged over all of the experiments is 0.59% in the streamwise direction and 0.87% in the transverse direction. A conservative estimate of PIV measurement error of 0.1 pixel displacement would correspond to 0.15 m/s which would change the turbulent intensity by 0.05%.

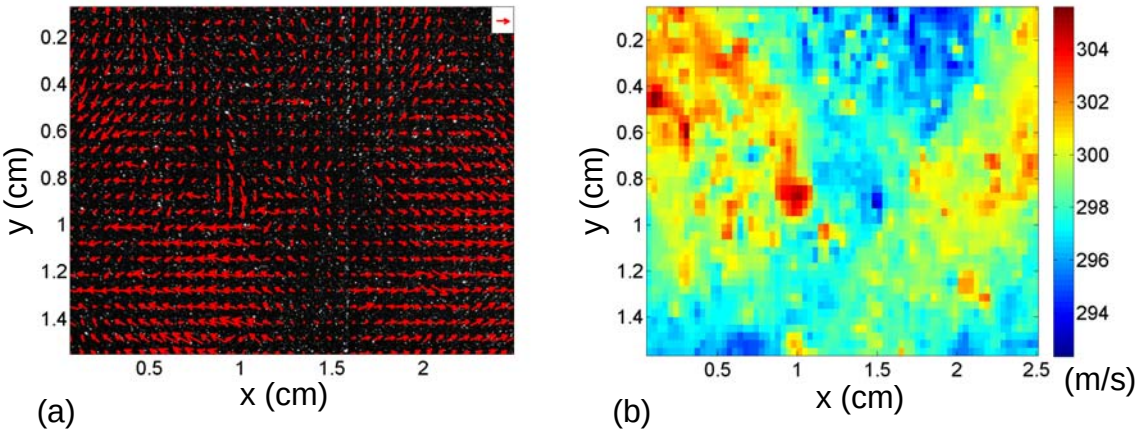

Figure 15: PIV results. (b) The vector field from a PIV analysis with the mean velocity subtracted. The reference vector in the top right corner is 5 m/s. The background is the original particle image. (b) The velocity magnitude of the image in (a).

The second source of error comes from the ability of the particles to track the flow. The particles have a stated size of 50 nm but may agglomerate to sizes much larger than this [35]. A way of indirectly determining the particle size is by observing the lag distance behind the flow. Figure 16 shows an experiment where the bottom gas was seeded and the shock wave impulsively accelerated the interface to 390 m/s. The image shows that, while there are a handful of particles that fell behind the interface by ~ 1 cm, the majority of the particles are within 0.25 cm of the interface. Using this distance in a Stokes drag calculation, a particle size of 1.1 μm is found. Hjelmfelt and Mockros [36] analyzed the ability of a particle to follow the turbulence of a given frequency. With this particle size, a maximum turbulence frequency of 27 kHz is observable. From the eddy turnover frequency, $u_k k/2\pi$, obtained from the energy spectra data that will be discussed below, a maximum turbulent frequency of ~200 Hz is observed. Therefore these particles adequately follow all eddies in the post-shocked flow.

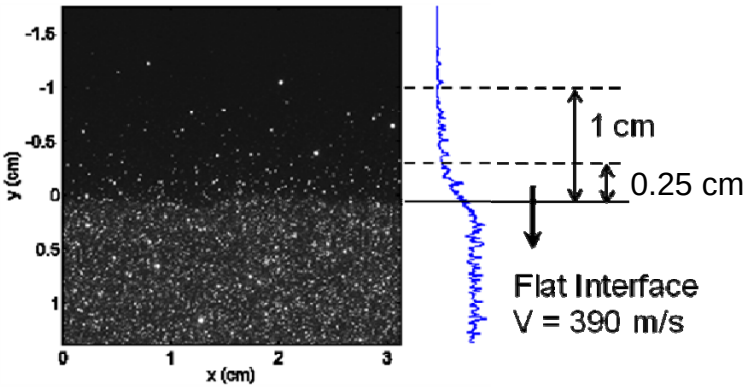

Figure 16: Particle lag after an impulsive acceleration. The initially flat interface was shock-accelerated to 390 m/s and some particles required a distance to accelerate to the gas velocity. Some particles are up to 1 cm behind the interface, while the majority of the particles are within 0.25 cm.

4.3 Fluctuating Kinetic Energy Spectra

The spectrum of turbulent kinetic energy is computed in both the *x* (transverse) and *y* (streamwise) directions. The procedure for the *x*-direction is as follows. The fluctuating velocity within a row of the velocity field data is obtained by subtracting off the mean velocity in this row. A discrete Fourier transform (DFT) of the fluctuating velocity is computed using a window function to reduce spectral leakage [37]. As in other experimental turbulence spectra measurements [36,37], a Hanning window function was chosen for computing the DFT. The total kinetic energy spectra are found by multiplying the transformed component by its complex conjugate and adding the energy from the other direction of velocity. An example of this energy spectrum is shown in the semi-log plot Figure 17, where the *x*-axis is the log of the wavenumber and the *y*-axis is the location of each row. This plot shows that the spectrum does change significantly throughout the domain. Each spectral component is averaged across the domain and combined with that of two other experiments of the same type (same time, location, and initial interface).

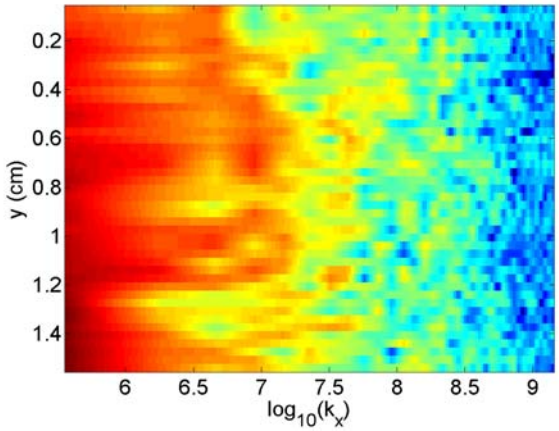

Figure 17: Semi-log plot of fluctuating kinetic energy. The y-axis is the physical dimension in the PIV image and the x-axis is log of the wavenumber. The energy spectrum does not change significantly throughout the height of the domain.

As already mentioned, data is taken at two times, referred to as early and late, and at two locations, referred to as near and far with respect to the interface. The experiments are conducted with an initial sinusoidal waveform imposed on the interface and with an initially flat interface, referred to as wave and flat experiments, respectively. Three experiments were conducted for each of these eight different scenarios, with a total of 24 experiments in all. The spectra shown in the following figures are averages from the three experiments.

Figure 18 shows the fluctuating kinetic energy spectra at the early time. The error bars represent the 95% confidence interval for the mean energy at that wavenumber across the entire velocity field from the three experiments of the same type. For most wavenumbers in the spectra, the k_y modes have a higher energy content than the k_x modes. This is true for both the initially flat interface and that with a waveform perturbation. This shows the anisotropy of the post-shocked turbulence. Because the turbulence is anisotropic, we do not expect a $k^{-5/3}$ scaling. The spectra have a slightly lower slope than -5/3 up until about 4×10^3 m^{-1}, after which the slope is steeper,

possibly signifying the beginning of the dissipative range. Since the initial turbulence spectrum is not known, the anisotropy may be due to the shock wave or the initial spectrum.

Near the interface in these early time experiments, the first few lower wavenumber modes in the k_x direction have a higher energy content when the waveform is present on the interface. In the k_y direction, and at higher wavenumber in the k_x direction, the flat interface spectra have a slightly higher energy content when compared to waveform experiments. The reason for these differences is not clear. Further from the interface the spectra from the interface with an initial wave perturbation have a higher energy content than that of the initially flat interface. A possible explanation for this is that the region further from the interface has more recently experienced a shock wave passing through it. The shock wave that reflects off the interface is deformed with a shape similar to the interface and distorts the flow field behind it as it returns to planar. The near location has had more time for these effects to dissipate away. It can also be seen that the spectra at the far location are larger in magnitude than that of the near location at this early time, which also suggests that dissipation is behind these differences. From this, we can expect that the differences in the far location will become less at later times.

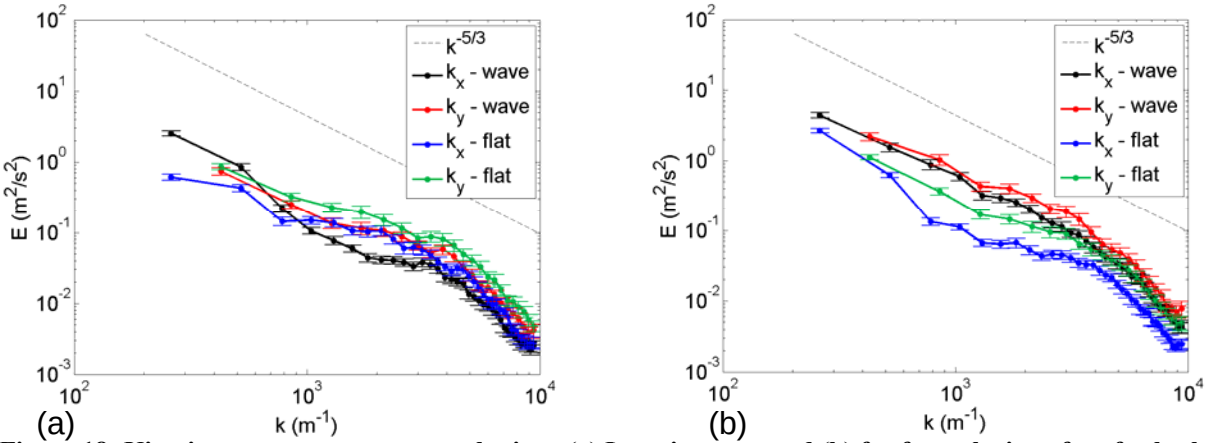

Figure 18: Kinetic energy spectrum at early time. (a) Location near and (b) far from the interface for both an interface with a waveform perturbation and a flat interface. The error bars signify the 95% confidence interval for the mean values.

The fluctuating kinetic spectra for the later time experiments are shown in Figure 19. In Figure 19(b), we see that, as expected, the differences in the kinetic energy spectra are reduced: the spectra from the experiments with an initial wave are nearly the same as that from the flat interface experiments. The k_y spectra are still larger than the k_x spectra so it appears that a return to isotropy will occur at larger times scales than are observed between these experiments. At the nearer location the spectra for the wavy interface in both directions are larger than those for the flat interface. The spectra in Figure 19(a) do not extend to the high wavenumbers that are obtained in the rest of the experiments because the PIV interrogation window size was doubled. At this location it appears that mixing between the two gases and boundary layer effects are causing refractive index gradients, known as aero-optical effects [40], to blur the image slightly, so a larger interrogation window was needed to include enough clear particles to get an accurate velocity measurement.

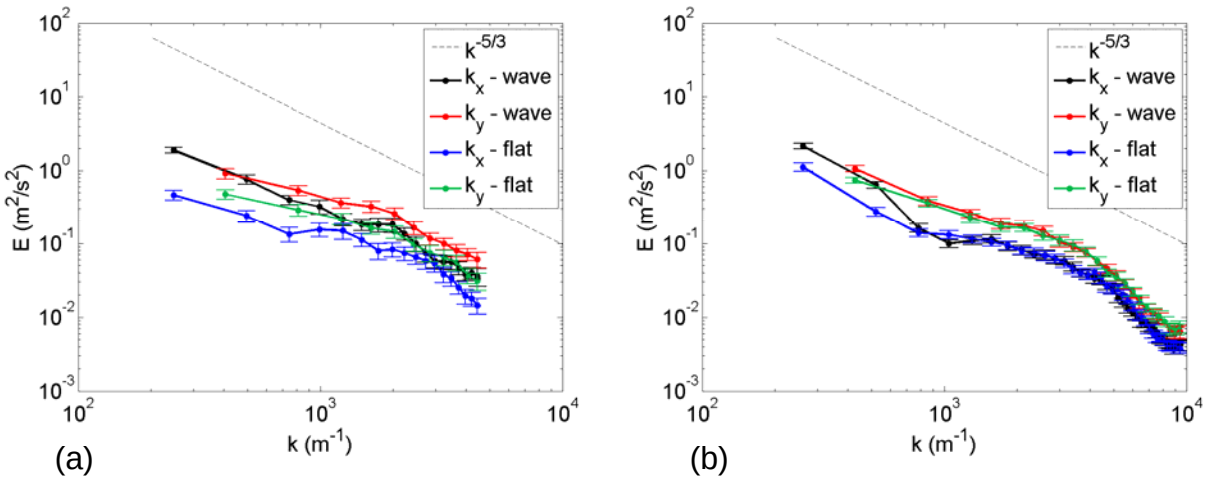

Figure 19: Kinetic energy spectrum at late time. (a) Location near and (b) far from the interface for both an interface with a waveform perturbation and a flat interface.

The change in the spectra over time is shown by combining Figure 18 and 7. Figure 20(a) shows that near the perturbed interface, the spectra at higher wavenumbers increase in energy content between the early and late times. At the location further from the interface, Figure 20(b), the energy content at all wavenumbers decreased from the early to the late time. These spectra seem to confirm our hypothesis, that the deforming interface will add kinetic energy near to it, while dissipation will dominate further from the interface.

Near the flat interface, Figure 21, the energy spectra stay nearly the same, decreasing slightly for a few wavenumbers. Far from the flat interface the spectra also stay roughly the same; the k_x spectra increases slightly at high wavenumber and decreases slightly at low wavenumbers. It was expected that a decrease in the energy spectra would have been observed in these figures, similar to that of Figure 20(b). What appears to be occurring is that the excess energy left behind by the distorted shock wave is quickly dissipated away. This rate of energy dissipation is higher than the dissipation of the initial turbulence, which is presumably present in the flat interface spectra and does not change significantly.

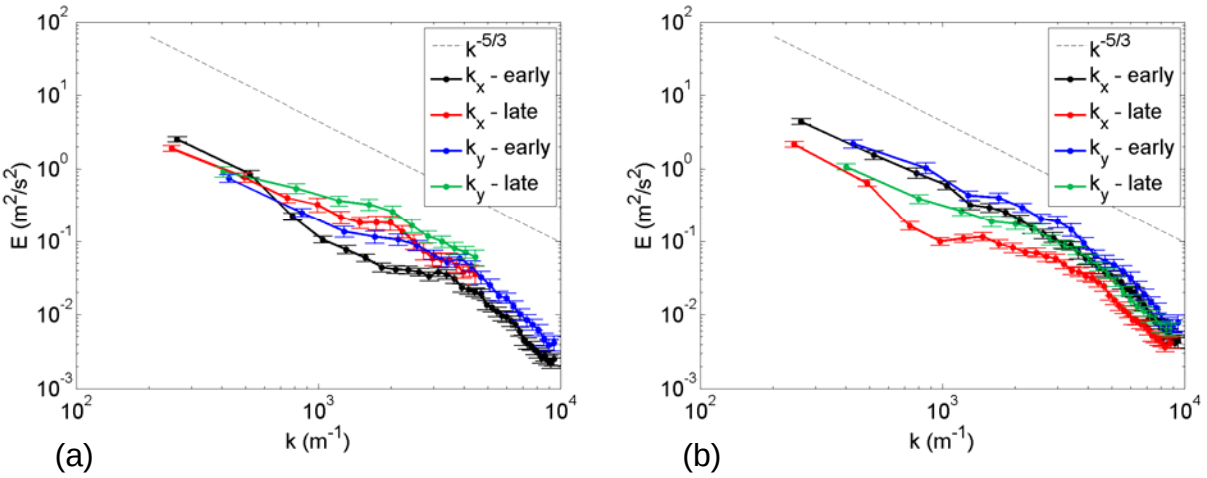

Figure 20: Kinetic energy spectra for wave interface. The spectra at different times are compared at the (a) near and (b) far locations.

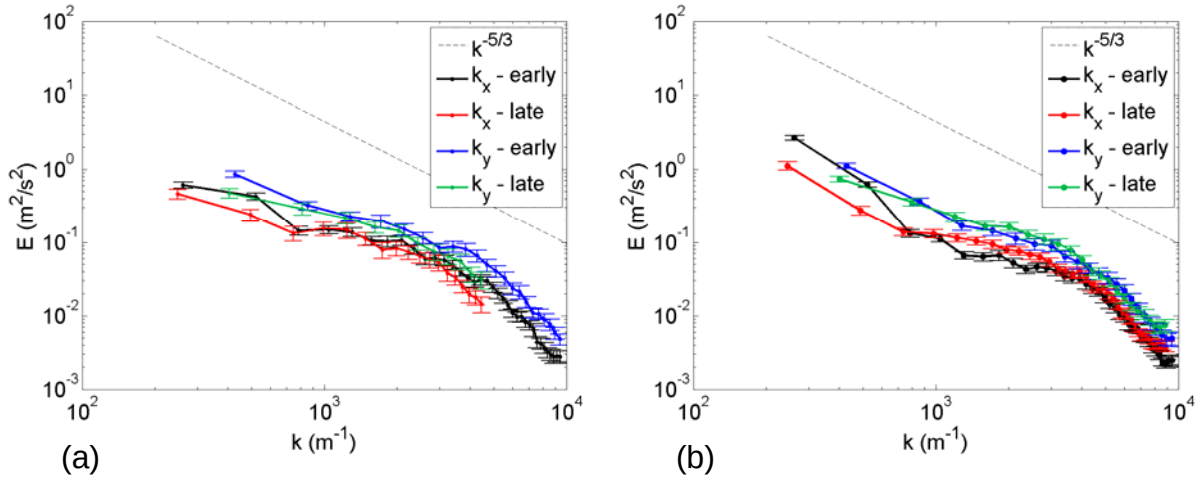

Figure 21: Kinetic energy spectra for flat interface. The spectra at different time are compared at the (a) near and (b) far locations.

4.4 Simulation

To confirm the trends discussed in these experiments, a single mode, two-dimensional simulation was preformed. The initial conditions in the simulation were set to match the initial Mach number, wavelength and amplitude of the experiment. No initial velocity, other than the shocked gas, was present in the initial setup. The simulation uses 10th order spatial differencing with a 4th order Runge-Kutta temporal integration. An artificial fluid large eddy simulation (LES) scheme is used to provide stability along with the appropriate numerical dissipation [41]. The resolution in the simulation is □/256 = 348 μm, providing a similar resolution to the PIV data.

The fluctuating energy spectra are computed in regions chosen to be a similar distance from the interface as the locations observed in the experiments. The red region in Figure 22 spans the entire width of the domain. Since the *x*-boundaries in the simulation are periodic, the spectra in this region can be computed without the use of a window function. The green region is chosen to be the same size and location as in the experiments, but it is necessary to use a Hanning window function when computing the DFT.

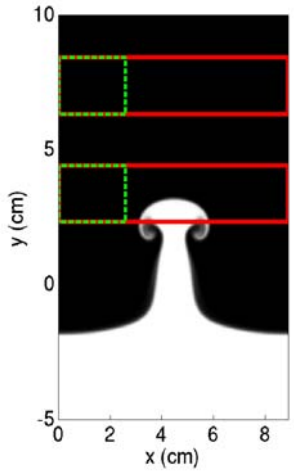

Figure 22: Analysis regions in simulation. A field plot of N_2 (black) and SF_6 (white) is plotted from the simulation at 0.9 ms and the two analysis regions are shown. The Fourier transform in the full width of the domain (red) allows us to take advantage of the periodic boundary conditions. The green region is chosen to match the region investigated in the experiment.

Figure 23 show the spectra computed using the full width of the domain. The trends of interest in these spectra are an increase in spectral energy at the near location and a decrease in energy far from the interface. These trends appear to be present for most wavenumbers. A hump in the spectrum is present at the earliest time near k_x = 2000 m^{-1} at both locations and dissipates away. It is not clear where this feature comes from. Since the simulation is 2-dimensional, a k^{-3} spectrum is expected for fully developed turbulence [42] and is observed at the later time near the interface.

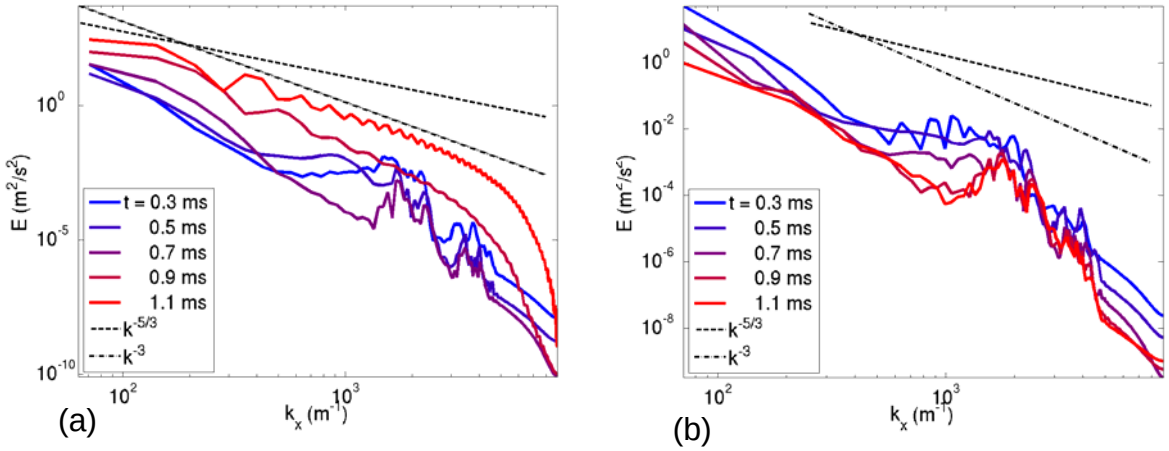

Figure 23: Kinetic energy spectra from simulation using full domain width. Five energy spectra are plotted from different times to show changes (a) near and (b) far from the interface.

Figure 24 shows the spectra computed within the green box in Figure 22 and using a Hanning window function. Near the interface at this location the energy spectra decrease for the first few time steps and then increase over the last three time steps. The hump in the spectra is also present at this location and is gone by the later times. Further from the interface, nearly all modes decrease in energy at each time step.

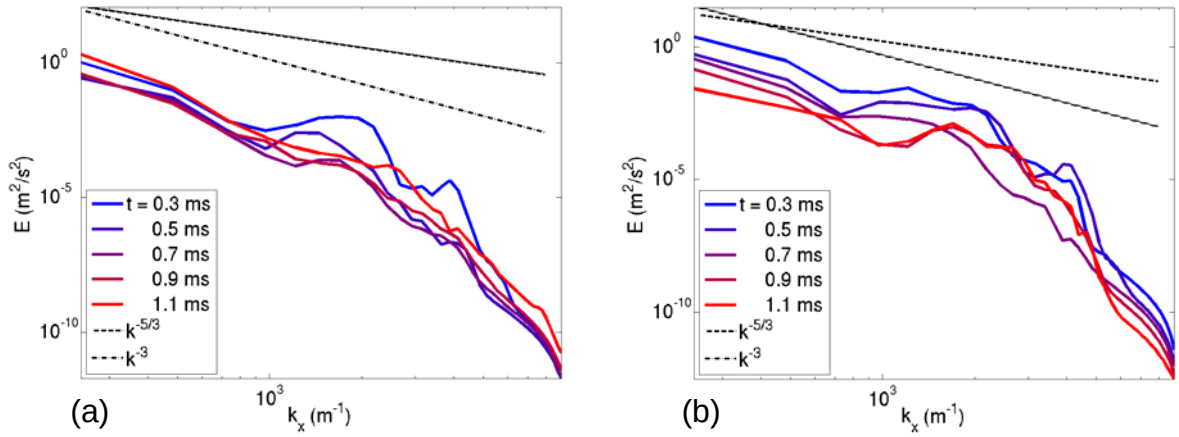

Figure 24: Kinetic energy spectra from the simulation using the smaller region. The smaller region of interest (a) near and (b) far from the interface is chosen to match the location observed in the experiments. The energy spectra from five times are shown.

The simulation data appear to confirm the results shown in the experiments, that energy production occurs near the interface and dissipation dominates further from the interface. A 3-dimensional simulation is necessary to make quantitative comparisons to the experiments, as the physics of the energy cascade are fundamentally different in three dimensions. At the present time, a 3-D simulation has not been computed because of the significant computational cost required to resolve the necessary scales.

4.5 Summary and Discussion

This work investigated the energy spectra at small scales in the presence of a shock-accelerated interface and the effect that the Richtmyer-Meshkov instability has on the spectra. It is observed that, near the perturbation, the energy spectra increase in time as energy from the large scales of the perturbation cascades towards smaller scales. Further from the interface the presence of the perturbation is observed, as the fluctuating kinetic energy is higher than that of a flat interface. Later in time these differences are no longer present, as dissipation has reduced the excess energy deposited by the distorted reflected shock wave.

It is unclear as to why the spectra with a flat interface stay largely unchanged between the two times. It is possible that dissipation effects will be enhanced and more easily observed in a flow with higher turbulence intensity. When the flow becomes isotropic is not known and experiments later in time are needed to investigate this.

This is, as far as the author is aware, the first time that the influence of the RMI on the kinetic energy spectrum has been experimentally investigated at different locations from the interface. Since this influence extends beyond just the mixing region, it is possible that applications concerned with the RMI will need to consider more than just the mixing width.

5.0 Richtmyer-Meshkov Instability on a Low Atwood Number Interface after Reshock

5.1 Background

An interface between two gases that is accelerated by a shock wave is unstable regardless of the path the shock wave takes. If the shock wave travels from the light gas to the heavy one, perturbations on the interface will grow in amplitude. If the shock travels in the reverse direction, the vorticity will be of the opposite sign than the previous case, and the perturbation will first compress and reverse phase, and then grow in the opposite direction. These cases can be combined in a shock tube by allowing a once-shocked interface to be reshocked by a shock wave that reflects from the end wall.

Shock tube experiments investigating the RM instability after reshock have the advantage that the interface is nearly stationary after reshock, allowing the interface to be viewed in the same window for a longer period of time. At the time of reshock, the interface has grown in amplitude. When the reflected shock wave passes through this larger interface, the vorticity deposited will be much larger than that from the first shock interaction. The larger vorticity will cause the amplitude growth rate after reshock to be several times larger in magnitude than prior to reshock.

Previous shock tube experiments investigating the RM instability after reshock have obtained full field images using either planar imaging [16,41] or schlieren [22,42]. The amount of data collected for each experiment is limited by the laser pulse rate or the camera frame rate. The current work uses two continuous laser beams to acquire high speed amplitude measurements. This new method has two advantages: data can be taken with higher temporal resolution and the measurements are taken from the same plane as the planar imaging. The experimental results are compared with models and a simulation. Additionally a new model is introduced for circulation and amplitude growth rate estimates for single or multiple shock waves.

5.2 Experimental Setup

The interface is created in the shock tube by flowing pure argon gas from below and a 50-50% volume fraction mixture of helium and argon from above [45]. The gases meet to form a stagnation plane and exit through slots in the shock tube due to a pressure differential provided by a vacuum pump. The slots are centered in a pair of 5.08×25.4 cm^2 rectangular pistons that are embedded in the walls. After the gases have flowed for a sufficient time to ensure purity, the pistons are oscillated at 1.25 Hz for 14 revolutions to create a standing wave with an initial amplitude of 0.35 cm and a wavelength of 19.4 cm. The interface has an Atwood number $\left(A = \left(r_2 - r_1\right)/\left(r_2 + r_1\right)\right)$ of 0.29. A sample initial condition image is shown in Figure 25 along with a modal decomposition, showing that the perturbation is primarily a single mode.

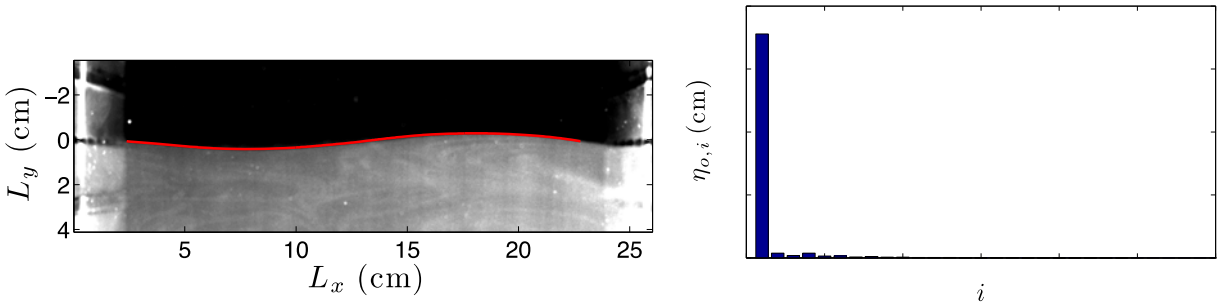

Figure 25: Initial condition image and modal content. L_y is the streamwise region of interest for the initial condition and L_x is the spanwise dimension.

Before the experiment begins, the driver is filled to 85% of the diaphragm rupture pressure. Approximately 300 ms before the acceleration of the desired standing wave occurs, a high-pressure boost tanks opens, filling the driver with gas, and rupturing the diaphragm. The long length of the shock tube ensures a planar shock wave by the time it reaches the interface. The incident Mach 1.92 shock wave transmits through the interface and reflects from the end wall as a Mach 1.70 shock wave.

Flow visualization is performed by seeding the bottom gas with Al_2O_3 particles using a fluidized bed. Four lasers enter from the bottom of the tube, illuminating a plane halfway between the front and back walls. Planar images are acquired using a KrF excimer laser for an initial condition image and a dual cavity Nd:YAG laser for post-shocked/re-shocked images. The initial condition image is recorded on a cooled Andor CCD camera and a pair of post-shocked or re-shocked images are captured with a Lavision PIV camera.

In addition to planar imaging, a high speed diagnostic is implemented using two continuous argon ion laser beams entering from the bottom of the tube and positioned below the spike and bubble of the initial condition. The Mie scattering signals from the laser beams are recorded with two high speed cameras from Redlake and IDT at 116,509 Hz. The data from these cameras are used to track the transmitted and reflected shock waves and observe the interface as it travels through the viewing window. This setup allows for an experimental *x-t* diagram to be constructed from each camera. Amplitude growth over time can then be determined using the *x-t* diaphragms from the two cameras.

5.3 Experimental Results

A set of planar images is shown in Figure 26. The first image is taken 0.10 ms before the reflected shock wave has reached the interface. The interface has grown to 0.92 cm in amplitude. The first image shows a few stray particles up to a centimeter above the interface. The seeding method allows for a distribution of particles of various sizes, with larger particles taking longer to accelerate in the presence of high velocity gradients, such as the passage of the incident shock wave. The maximum particle size is estimated to be 2.1 μm. This value is calculated using the distance lag of the particles in Figure 26(a) and the velocity of the interface [35]. The defined contour of the interface suggests that most particles are of sufficiently small size to show no lag.

The images after reshock, Figure 26(b)-(h), initially show the interface compresses in amplitude at 0.06 ms and then reverses in phase by 0.61 ms. Later in time, after 0.86 ms, secondary

instabilities can be seen arising on the interface, predominantly at the mid location between the spike and the bubble. The rarefaction that reflects from the end wall is expected to be arriving at the interface after the 0.86 ms image.

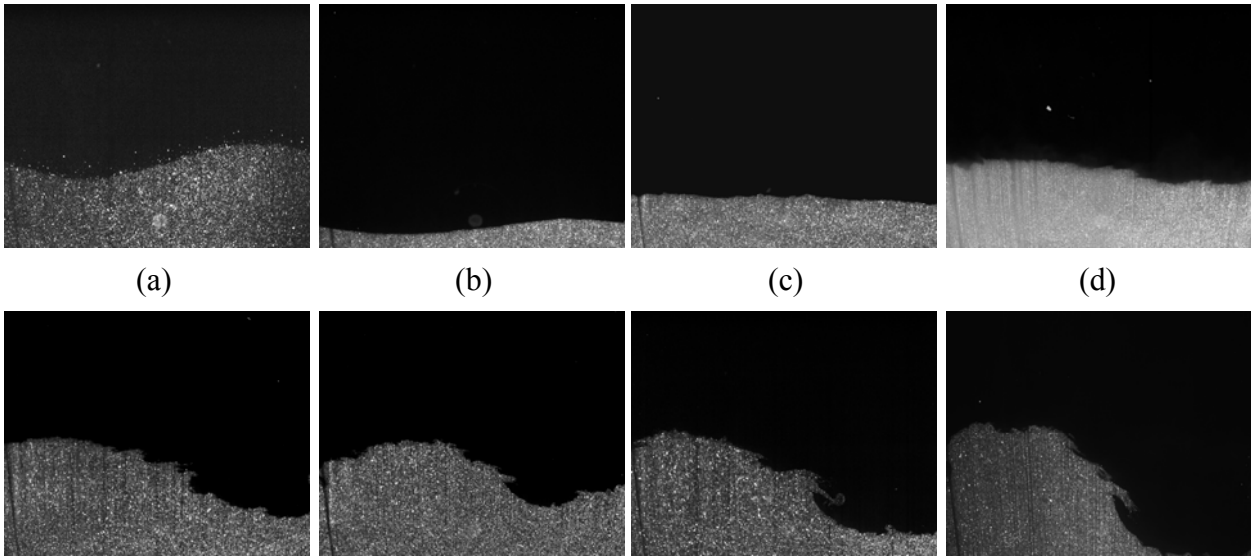

Figure 26: Planar images of the instability. Image (a) was taken 1.86 ms after being accelerated by the first shock wave but 0.10 ms before being reshocked. The following images all occur after being reshocked with the time after reshock being (b) 0.06 ms, (c) 0.34 ms, (d) 0.61 ms, (e) 0.86 ms, (f) 1.09 ms, (g) 1.34 ms, and (h) 1.63 ms.

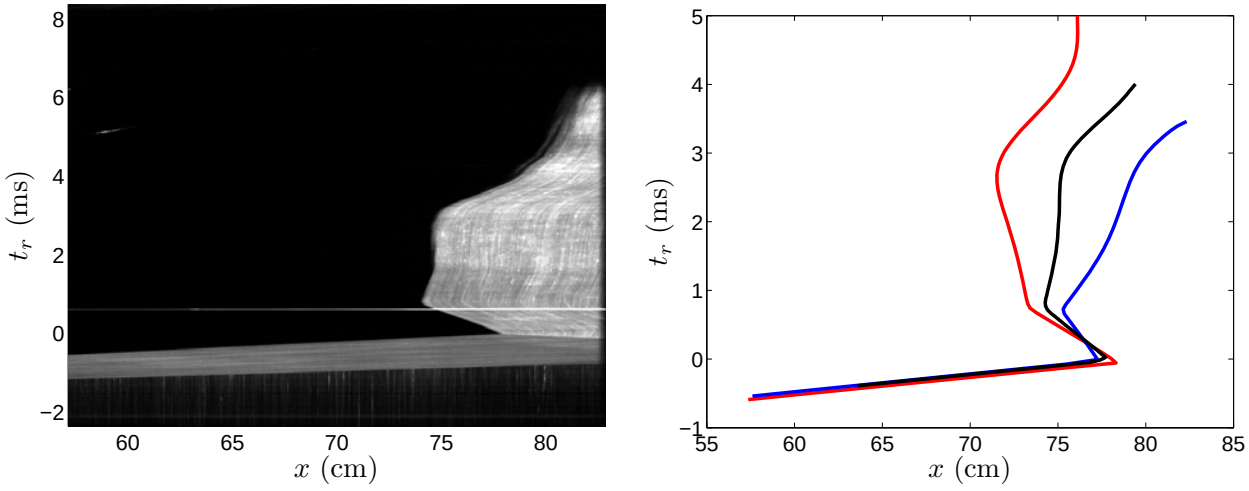

Figure 27: Experimental x-t diagram from an (a) initially flat interface showing the scattered light signal, revealing the transmitted and reflected shock waves and the path of the interface. (b) Experimental x-t diagrams showing the interface location for a bubble (blue) and spike (red) from a single experiment. Also plotted is the interface location from an initially flat experiment (black).

Figure 27(a) shows an example of an experimental *x-t* diagram taken from an initially flat interface. In the beginning ($t_r \approx$ -2 ms), unshocked seeded argon can be seen. At $t_r \approx$ -1 ms the transmitting shock can be seen traveling through the diagram, where it compresses the seeded argon, causing the scattered signal to intensify. At $t_r \approx 0.5$ ms the interface travels through the diagram until it is reshocked at $t_r = 0$ m and 78 cm from its initial location. The reshocked interface then travels upward in the tube (to the left in the diagram) until the rarefaction wave that reflects off the bottom wall causes the interface to become nearly stationary. At $t_r \approx 0.6$ ms the pulse from the Nd:YAG laser can be seen. At $t_r \approx 3.5$ ms a wave that has reflected off the contact surface between the driver gas and the driven gas causes the interface to move downward. Figure 27(b) shows the locations for a spike and bubble from a single experiment compared with that from an initially flat interface experiment.

Model Comparison

Amplitude vs time after reshock of six experiments are extracted from the experimental *x-t* diagrams and plotted in Figure 28. The differences in initial condition amplitudes resulted in the amplitude before reshock to range from 0.82 cm to 1.76 cm. The variation in the amplitude growth rates due to the different initial conditions allows for a comparison to several reshock growth rate models. Brouillette and Sturtevant [46] extended Richtmyer's impulsive model:

$$\dot{\eta} = k\eta_0^+ \Delta v A^+ \tag{16}$$

to include multiple shock interactions through a summation of the impulsive growth of each:

$$\dot{\eta} = k \sum_i \eta_i \Delta v_i A_i^+ . \tag{17}$$

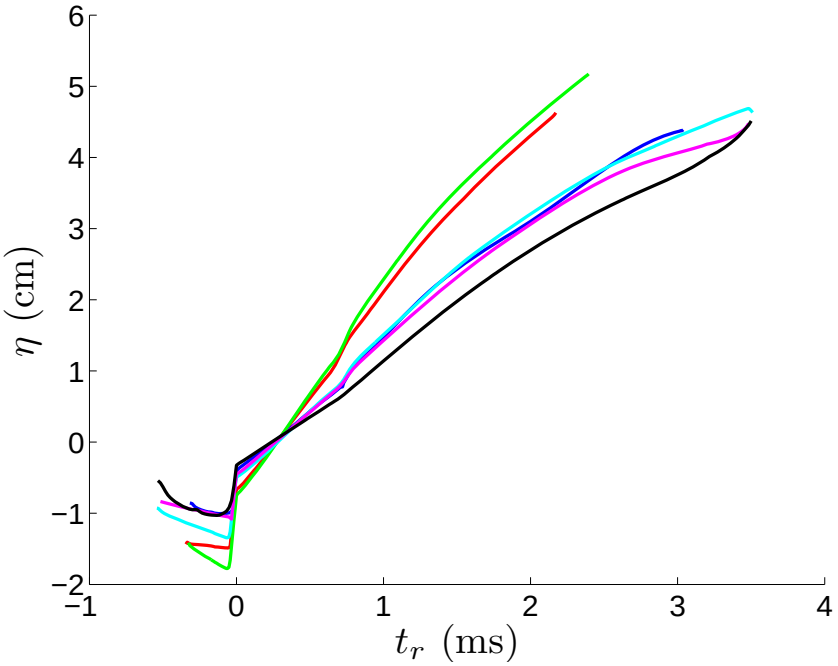

Figure 28: Amplitude vs. time after reshock for six experiments. The amplitude before reshock is 0.82 cm (black), 0.97 cm (blue), 1.05 cm (magenta), 1.33 cm (cyan), 1.48 cm (red), and 1.76 cm (green).

Mikaelian [47] extended the phenomenological model of the Rayleigh-Taylor mixing layer experiments and simulations of Read [48] and Youngs [49] to the Richtmyer-Meshkov instability after reshock:

$$\dot{\eta}=0.14\Delta v A^{+}. \tag{18}$$

Although this model describes three-dimensional multimode interfaces, it has been shown previously to provide a good estimate of amplitude growth of single mode interfaces after reshock [50].

Jacobs and Sheeley [51] showed that for a low A interface the circulation on a half-wavelength is related to the amplitude growth rate by

$$\dot{\eta}_0^{+}=-\frac{k}{4}\Gamma. \tag{19}$$

We use this relation with a model estimating the circulation deposited on the interface to produce a new growth rate model. The velocity field around the interface as the incident shock is refracting can be approximated by dividing the region into the corresponding values calculated from one-dimensional gas dynamics, shown in Figure 29(a). The circulation deposited on the interface can be modeled by performing a line integral about a closed contour, P, forming a box around a half-wavelength:

$$\Gamma = \int \omega \cdot d\mathbf{A} = \oint_P \mathbf{v} \cdot d\mathbf{s}.$$

This line integral, shown in Figure 29(a), becomes

$$\Gamma=u_{2r}y_1+u_{2r}y_2+u_1y_3-u_2y_4-u_2y_5, \tag{20}$$

where

$$y_1=u_t t+W_r t, y_2=W_t t-u_t t, y_3=W_i t-W_t t,$$

$$y_4=W_r t, \text{and } y_5=W_i t, \text{and } t=\frac{2\eta_0}{W_i}.$$

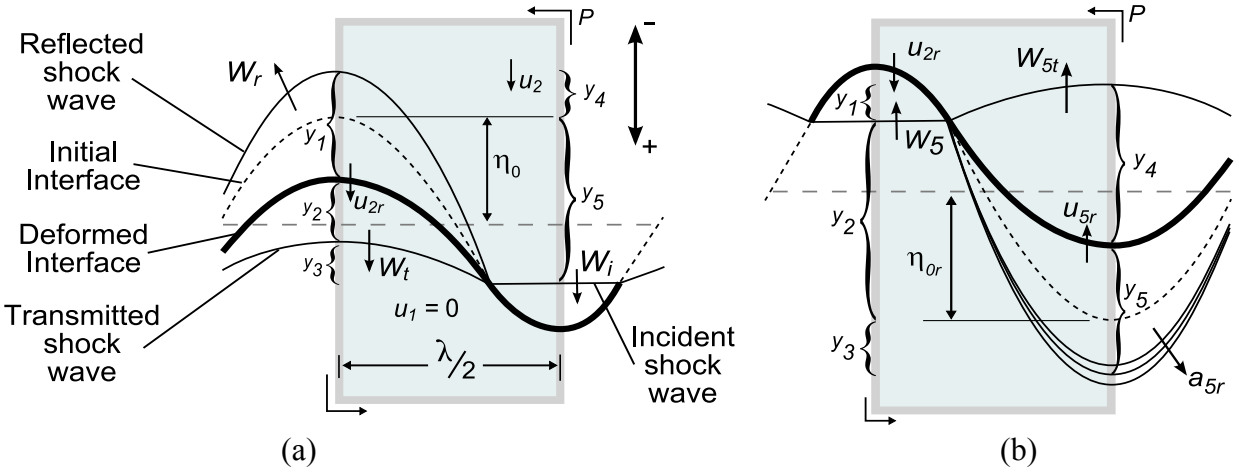

Figure 29: Diagram of a shock wave passing through a light-over-heavy sinusoidal interface. (a) Single shock interaction: incident shock wave is propagating downward through an unshocked interface. (b) Reshock interaction: reflected shock wave is traveling up through the once-shocked interface.

The time is taken to be the time it takes for the incident shock wave to travel across the entire interface, i.e. $t=2\eta_0/W_i$. Combining Eqs. (19) & (20), and noting that $u_1=0$, yields an estimate for the growth rate due to the incident shock wave.

$$\dot{\eta}_0^+ = -\frac{k\eta_0}{2W_i}\left[u_{2r}\left(W_r+W_t\right)-u_2\left(W_i+W_r\right)\right] \tag{21}$$

A similar approach is applied to the reshocked interface, shown in Figure 29(b). In this case, the wave reflects off the interface as a rarefaction wave, which we can estimate to be traveling at the sound speed in that medium. The line integral becomes

$$\Gamma = u_{2r}y_1+u_5y_2+u_5y_3-u_{5r}y_4-u_{5r}y_5,$$

where,

$$y_1=W_{5t}t-W_5t, y_2=W_5t, y_3=a_{5r}t,$$

$$y_4=W_{5t}t-u_{5r}t, y_5=a_{5r}t+u_{5r}t, \text{ and } t=\frac{2\eta_{0r}}{u_{2r}-W_5}.$$

We can simplify these equations by noting that $u_5=0$. The signs of all velocities are taken to be positive downwards in Figure 29(a,b). Since the vorticity from the two interactions will add to the net circulation, the two growth rates should be added to provide the net growth rate after reshock. The final growth rate after reshock is

$$\dot{\eta}_{0r}^+ = \dot{\eta}_0^+ - \frac{k\eta_{0r}}{2\left(W_5-u_{2r}\right)}\left[u_{5r}\left(a_{5r}+W_{5r}\right)-u_{2r}\left(W_{5t}+W_5\right)\right]. \tag{22}$$

The experimental growth rates divided by the growth rate predicted by each of the models are shown in Figure 30. The time is scaled by the wave number and the model growth rate. Figure 30(a) uses the growth rate determined by the Brouillette and Sturtevant model, Eq. (2). Reshock occurs at $\tau = 0$ and the rarefaction wave that reflects off the end wall interacts with the interface at $\tau \approx 0.3$. At a time halfway between the reshock and rarefaction, the model underestimates the growth rate on average by 59%. It is interesting to note, however, that the growth rate of only the interaction of the second shock, shown in Figure 30(b), does accurately describe the growth rate of the experiments after reshock by overestimating the growth by only 7%. The model growth rate from the Mikaelian model, Eq. (18), is used in the scaling of Figure 30(c). Here we find the model does not collapse the growth rates well, but it does roughly match the growth rate of the average of the experiments. The average growth rate is overestimated by 12%. The 1-D circulation based growth rate model, using Eq. (22), is used in the scaling of Figure 30(d). The model overestimates the growth rate on average by 19%. It performs best when the amplitude before reshock is larger: for the $\eta_{0r}^- = 1.75$ cm experiment, the model was above the experimental growth rate by 2%.

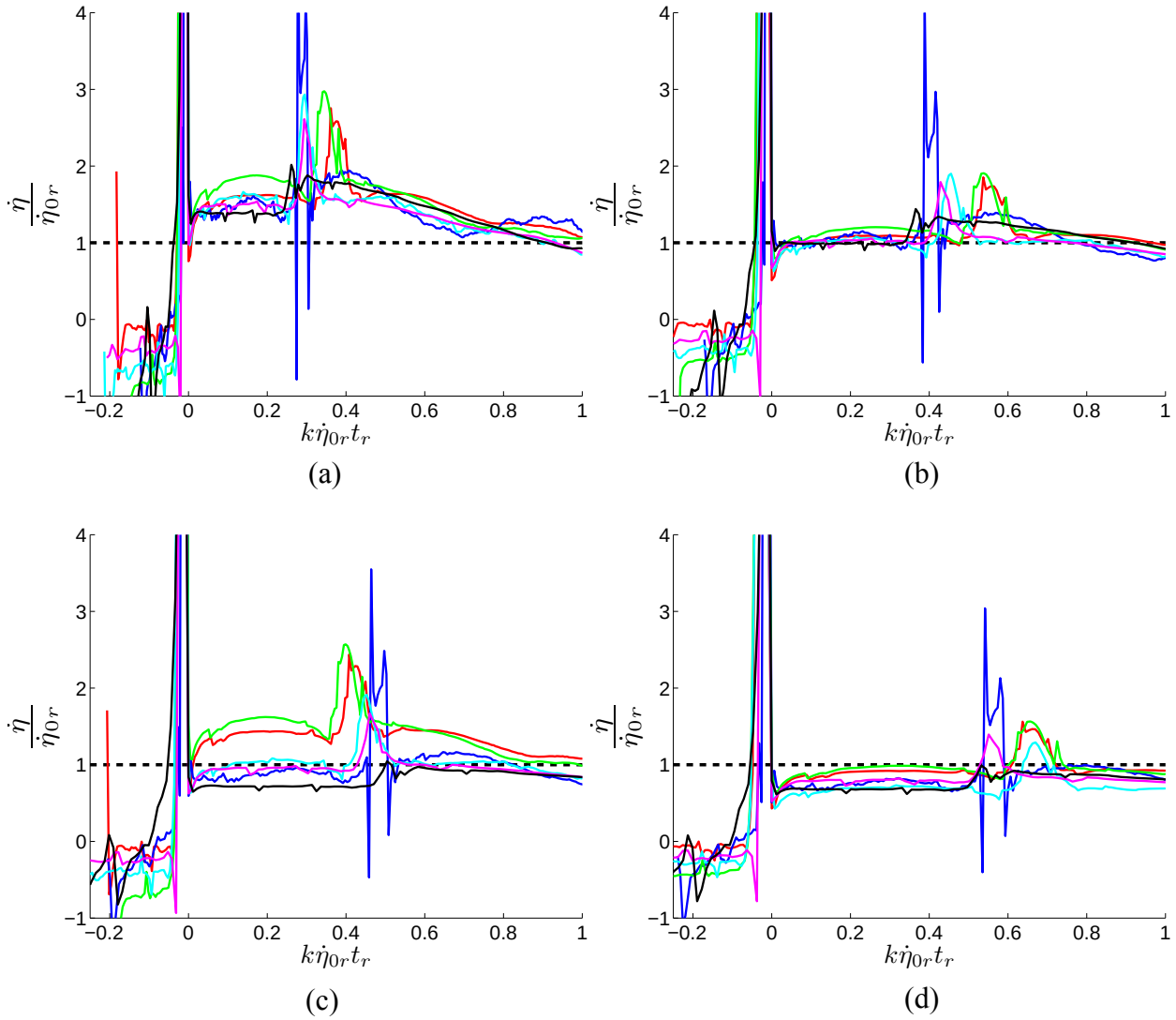

Figure 30: Experimental amplitude growth rate divided by the model growth rate. The model growth rates used are from (a) the Brouillette-Sturtevant model, (b) the impulsive model using only reshock, (c) the Mikaelian model, and (d) the 1-D circulation based model.

The models vary in their ability to collapse the experimental growth rate to a single curve. The maximum difference in the normalized growth rates between the different experiments

$$\left(\frac{\dot{\eta}_{\text{exp}}}{\dot{\eta}_{0r}}\right)_{\text{max}} - \left(\frac{\dot{\eta}_{\text{exp}}}{\dot{\eta}_{0r}}\right)_{\text{min}}$$

is largest for the Mikaelian model at 0.90. This model does not contain a parameter for the initial amplitude, so experiments with high initial amplitude are growing faster than the model and the opposite for smaller initial amplitude experiments. The Brouillette and Sturtevant model collapses the experimental data better, with a maximum difference in normalized growth rate of 0.49. The 1-D growth rate model provides the best data collapse, with a maximum difference in normalized growth rate of 0.30.

5.4 Numerical Simulation

A numerical simulation of the average experimental conditions was performed using the hydrodynamics code *Raptor*, developed at LLNL, that solves the 2-D compressible Euler equations on a fixed (Eulerian) grid. The shock-capturing scheme uses a higher order Godunov solver to handle the shock propagation and suppress spurious oscillations near the discontinuity. Two levels of adaptive mesh refinement are applied to density gradients and along the interface with ratios of 4 and 4. The finest resolution has 512 cells per shock tube width (0.50 mm/cell).

The initial condition is a single mode sine wave based on the average amplitude and wavelength of the experiments. The interface was given a hyperbolic tangent diffusion thickness to match the calculated value of 1.42 cm [45]. The domain is initialized from the stationary state to capture all shocks and waves that arise during the experiment.

The amplitude growth rate from the simulation is compared with that from an experiment with a similar initial condition in Figure 31(a). The growth rate after reshock and after the reflected rarefaction are nearly identical, while the growth rate during the reflected rarefaction peaks higher for the experiment, both the simulation and experiment show the same trend. The 1-D model overestimates the growth rate after reshock of the simulation by 7%.

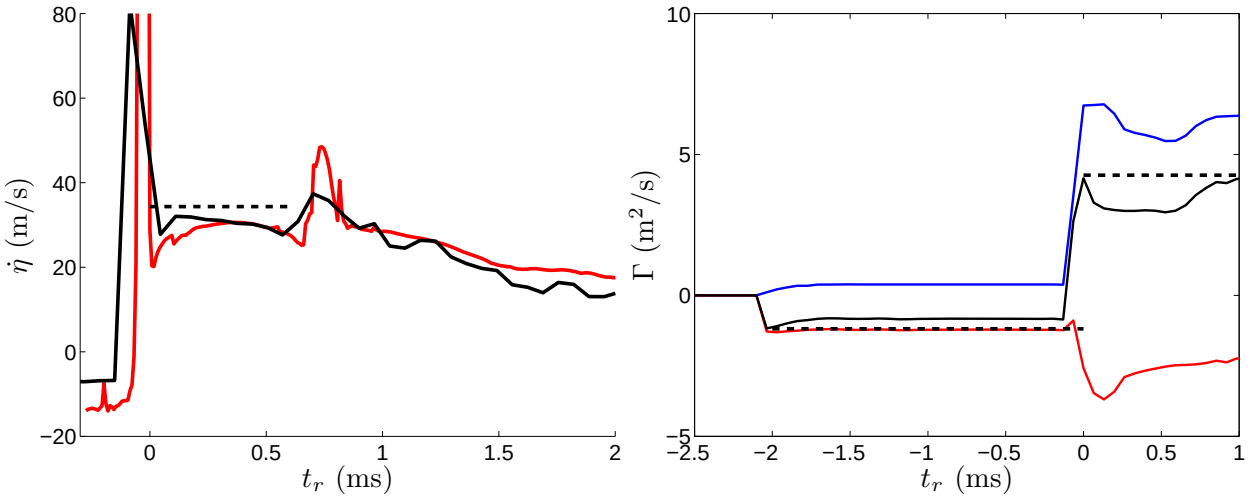

Figure 31: Simulation results comparing (a) the amplitude growth rate from the simulation (black) with that from a similar experiment (red) and the 1-D model (dashed). (b) Circulation over a half wavelength from 1-D model (dashed) and the simulation: Γ_+ (solid-blue), Γ_- (solid-red), and Γ_{net} (solid-black).

The results of the simulation allow for a direct comparison between the circulation from the 1-D model and that in the simulation. The circulation over a half-wavelength is integrated from the vorticity field and plotted in Figure 31(b). The net circulation of the simulation is initially within about 2% of the circulation predicted by the model after the first shock. As the instability develops further in time the circulation becomes about 30% less in magnitude than the model prediction. After reshock the circulation initially is within 3% of that predicted by the model and becomes underestimated by about 40% as the instability develops in time. The model only predicts the initial baroclinic circulation deposition, so the drop in the magnitude of the circulation as the instability develops in time is not expected to be reproduced by the model. The fact that the amplitude growth rate predicted by the model is higher than that seen in the

experiment and simulation suggests that this reduction in circulation could be an important parameter in the amplitude growth rate.

6.0 Summary and Conclusion

A statistically repeatable broadband initial condition was created for the Richtmyer-Meshkov instability. The initial condition is free of any interference from membrane or other physical obstruction and allows for high resolution imaging of the mixing structures within the turbulent mixing layer. When accelerated by a M=1.56 shock wave, the helium+acetone over argon mixing layer exceeds the transition to turbulent mixing threshold of $Re=2x10^4$. Qualitatively, turbulent mixing appears to be occurring by the latest time images, but PDFs of mole fraction do not show a more homogeneous mixture. It is possible that the interface needs more time to transition than available in these experiments. The energy spectrum at the late time appears to show evidence of an inertial range and PDFs of the angle of the mixing/dissipative structures show that the mixing layer is nearly isotropic by the late time.

The measurements of turbulent kinetic energy showed that the perturbations influence the spectrum a relatively far distance from the interface. When compared with the energy spectrum above a flat interface, the presence of the sine wave perturbation causes an increase in the kinetic energy spectrum. This increased energy is short lived, as dissipation reduces the excess energy to the level observed with the flat interface. Closer to the interface, the energy spectra at the small scales observed in these experiments increase in time due to the cascade of energy from the large scales of the perturbation.

Finally, the single mode perturbation growth after reshock was investigated using a new high-speed technique. A pair of continuous laser beams and high-speed cameras was used to record the position of the interface at over 100 kHz. This information is used to produce an experimental x-t diagram for the bubble location and the spike location. The experimental data was used to test a new model for reshock amplitude growth rate based on the estimated circulation deposited by the shock interaction. The model collapsed the experimental reshock growth rate slightly better than several other reshock models.

7.0 References

[1] R. D. Richtmyer, "Taylor instability in shock acceleration of compressible fluids," *Communications on Pure and Applied Mathematics*, vol. 13, no. 2, pp. 297-319, 1960.

[2] E. E. Meshkov, "Instability of a shock wave accelerated interface between two gases," *NASA Technical Translation*, vol. 13, pp. 1-14, 1970.

[3] J. D. Lindl et al., "The physics basis for ignition using indirect-drive targets on the National Ignition Facility," *Physics of Plasmas*, vol. 11, no. 2, p. 339, 2004.

[4] K. Kifonidis, T. Plewa, L. Scheck, H.-T. Janka, and E. Müller, "Non-spherical core collapse supernovae," *Astronomy and Astrophysics*, vol. 453, no. 2, pp. 661-678, Jul. 2006.

[5] F. Marble, G. Hendricks, and E. Zukoski, "Progress toward shock enhancement of supersonic combustion processes," in *AIAA, SAE, ASME, and ASEE, Joint Propulsion Conference, 23rd, San Diego, CA*, 1987, pp. 1-8.

[6] M. H. Anderson, B. P. Puranik, J. G. Oakley, P. W. Brooks, and R. Bonazza, "Shock tube investigation of hydrodynamic issues related to inertial confinement fusion," *Shock Waves*, vol. 10, pp. 377-387, 2000.

[7] M. M. Marinak, S. W. Haan, T. R. Dittrich, R. E. Tipton, and G. B. Zimmerman, "A comparison of three-dimensional multimode hydrodynamic instability growth on various National Ignition Facility capsule designs with HYDRA simulations," *Physics of Plasmas*, vol. 5, pp. 1125-1132, 1998.

[8] G. Dimonte and M. Schneider, "Density ratio dependence of Rayleigh–Taylor mixing for sustained and impulsive acceleration histories," *Physics of Fluids*, vol. 12, p. 304, 2000.

[9] M. Vetter and B. Sturtevant, "Experiments on the Richtmyer-Meshkov instability of an air/SF6 interface," *Shock Waves*, vol. 4, pp. 247-252, Mar. 1995.

[10] G. Dimonte and M. Schneider, "Turbulent Richtmyer-Meshkov instability experiments with strong radiatively driven shocks," *Physics of Plasmas*, vol. 4, no. 12, pp. 4347-4357, 1997.

[11] A. W. Cook and P. E. Dimotakis, "Transition stages of Rayleigh–Taylor instability between miscible fluids," *Journal of Fluid Mechanics*, vol. 443, pp. 69–99, 2001.

[12] K. A. Buch and W. J. . Dahm, "Experimental study of the fine-scale structure of conserved scalar mixing in turbulent shear flows. Part 1. Sc>>1," *J. Fluid Mech*, vol. 317, pp. 21–71, 1996.

[13] L. K. Su and N. T. Clemens, "The structure of fine-scale scalar mixing in gas-phase planar turbulent jets," *Journal of Fluid Mechanics*, vol. 488, pp. 1-29, Jul. 2003.

[14] B. R. Petersen, "High resolution passive scalar dissipation measurements in an internal combustion engine," 2009.

[15] C. Tomkins, S. Kumar, G. Orlicz, and K. Prestridge, "An experimental investigation of mixing mechanisms in shock-accelerated flow," *Journal of Fluid Mechanics*, vol. 611, pp. 131-150, 2008.

[16] B. D. Collins and J. W. Jacobs, "PLIF flow visualization and measurements of the Richtmyer Meshkov instability of an air/SF6 interface," *Journal of Fluid Mechanics*, vol. 464, pp. 113-136, Aug. 2002.

[17] P. E. Dimotakis, "The mixing transition in turbulent flows," *Journal of Fluid Mechanics*, vol. 409, pp. 69–98, 2000.

[18] A. W. Cook, W. Cabot, and P. L. Miller, "The mixing transition in Rayleigh–Taylor instability," *Journal of Fluid Mechanics*, vol. 511, pp. 333–362, 2004.

[19] P. E. Dimotakis, “Turbulent mixing,” *Annual Review of Fluid Mechanics*, vol. 37, pp. 329-356, 2005.
[20] P. L. Miller and P. E. Dimotakis, “Stochastic geometric properties of scalar interfaces in turbulent jets,” *Physics of Fluids A*, vol. 3, no. 1, pp. 168–177, 1991.
[21] G. Batchelor, *The theory of homogeneous turbulence*. Cambridge□;;New York: Cambridge University Press, 1982.
[22] S. A. Kaiser and J. H. Frank, “Imaging of dissipative structures in the near field of a turbulent non-premixed jet flame,” *Proceedings of the Combustion Institute*, vol. 31, no. 1, pp. 1515–1523, 2007.
[23] S. Pope, *Turbulent flows*. Cambridge [u.a.]: Cambridge Univ. Press, 2000.
[24] M. Brouillette, “The Richtmyer-Meshkov instability,” *Annual Review of Fluid Mechanics*, vol. 34, pp. 445–468, 2002.
[25] F. Poggi, M. H. Thorembey, and G. Rodriguez, “Velocity measurements in turbulent gaseous mixtures induced by Richtmyer–Meshkov instability,” *Physics of Fluids*, vol. 10, no. 11, pp. 2698-2700, Nov. 1998.
[26] P. Vorobieff, P. M. Rightley, and R. F. Benjamin, “Power-Law Spectra of Incipient Gas-Curtain Turbulence,” *Physical Review Letters*, vol. 81, pp. 2240-2243, Sep. 1998.
[27] P. Vorobieff, N. G. Mohamed, C. Tomkins, C. Goodenough, M. Marr-Lyon, and R. F. Benjamin, “Scaling evolution in shock-induced transition to turbulence,” *Physical Review E*, vol. 68, no. 6, p. 065301, Dec. 2003.
[28] A. W. Cook and Y. Zhou, “Energy transfer in Rayleigh-Taylor instability,” *Physical Review E*, vol. 66, no. 2, p. 26312, 2002.
[29] D. Besnard, F. H. Harlow, R. M. Rauenzahn, and C. Zemach, “Turbulent Transport Equations for Variable-Density Turbulence and Their Relationship to Two-Field Models.” 1992.
[30] G. Dimonte and R. Tipton, “K-L turbulence model for the self-similar growth of the Rayleigh-Taylor and Richtmyer-Meshkov instabilities,” *Physics of Fluids*, vol. 18, no. 8, p. 085101, 2006.
[31] Y. Andreopoulos, J. H. Agui, and G. Briassulis, “Shock Wave-Turbulence Interactions,” *Annual Review of Fluid Mechanics*, vol. 32, no. 1, pp. 309–345, 2000.
[32] C. E. Willert and M. Gharib, “Digital particle image velocimetry,” *Experiments in Fluids*, vol. 10, no. 4, Jan. 1991.
[33] K. Jambunathan, X. Y. Ju, B. N. Dobbins, and S. Ashforth-Frost, “An improved cross correlation technique for particle image velocimetry,” *Measurement Science and Technology*, vol. 6, no. 5, pp. 507-514, May 1995.
[34] F. Scarano, “Iterative image deformation methods in PIV,” *Measurement Science and Technology*, vol. 13, no. 1, pp. 1-19, 2002.
[35] A. Melling, “Tracer particles and seeding for particle image velocimetry,” *Measurement Science and Technology*, vol. 8, no. 12, pp. 1406–1416, 1997.
[36] A. T. Hjelmfelt and L. F. Mockros, “Motion of discrete particles in a turbulent fluid,” *Applied Scientific Research*, vol. 16, no. 1, pp. 149-161, 1966.
[37] F. J. Harris, “On the use of windows for harmonic analysis with the discrete Fourier transform,” *Proceedings of the IEEE*, vol. 66, no. 1, pp. 51–83, 1978.
[38] P. Doron, L. Bertuccioli, J. Katz, and T. R. Osborn, “Turbulence characteristics and dissipation estimates in the coastal ocean bottom boundary layer from PIV data,” 2010.

[39] C. D. Tomkins and R. J. Adrian, “Energetic spanwise modes in the logarithmic layer of a turbulent boundary layer,” *Journal of Fluid Mechanics*, vol. 545, p. 141, Dec. 2005.
[40] G. E. Elsinga, B. W. Van Oudheusden, and F. Scarano, “Evaluation of aero-optical distortion effects in PIV,” *Experiments in Fluids*, vol. 39, no. 2, pp. 246–256, 2005.
[41] A. W. Cook, “Artificial fluid properties for large-eddy simulation of compressible turbulent mixing,” *Physics of Fluids*, vol. 19, no. 5, p. 055103, 2007.
[42] R. H. Kraichnan, “Inertial Ranges in Two-Dimensional Turbulence,” *Physics of Fluids*, vol. 10, no. 7, p. 1417, 1967.
[43] B. J. Balakumar, G. C. Orlicz, C. D. Tomkins, and K. P. Prestridge, “Simultaneous particle-image velocimetry–planar laser-induced fluorescence measurements of Richtmyer–Meshkov instability growth in a gas curtain with and without reshock,” *Physics of Fluids*, vol. 20, no. 12, p. 124103, 2008.
[44] E. Leinov et al., “Experimental and numerical investigation of the Richtmyer-Meshkov instability under re-shock conditions,” *Journal of Fluid Mechanics*, vol. 626, pp. 449-475, May 2009.
[45] C. Weber, B. Motl, J. Oakley, and R. Bonazza, “Richtmyer-Meshkov Parameter Study,” *Fusion Science and Technolog*, vol. 56, no. 1, pp. 460-464, Jul. 2009.
[46] M. Brouillette and B. Sturtevant, “Growth induced by multiple shock waves normally incident on plane gaseous interfaces,” *Physica D*, vol. 37, no. 1-3, pp. 248-263, 1989.
[47] K. Mikaelian, “Turbulent mixing generated by Rayleigh-Taylor and Richtmyer-Meshkov instabilities,” *Physica D: Nonlinear Phenomena*, vol. 36, pp. 343-357, Aug. 1989.
[48] K. I. Read, “Experimental investigation of turbulent mixing by Rayleigh-Taylor instability,” *Physica D: Nonlinear Phenomena*, vol. 12, no. 1-3, pp. 45–58, 1984.
[49] D. L. Youngs, “Numerical simulation of turbulent mixing by Rayleigh-Taylor instability,” *Physica D: Nonlinear Phenomena*, vol. 12, no. 1-3, pp. 32 - 44, 1984.
[50] O. Schilling, M. Latini, and W. S. Don, “Physics of reshock and mixing in single-mode Richtmyer-Meshkov instability,” *Physical Review E*, vol. 76, no. 2, p. 26319, 2007.
[51] J. W. Jacobs and J. M. Sheeley, “Experimental study of incompressible Richtmyer–Meshkov instability,” *Physics of Fluids*, vol. 8, no. 2, pp. 405-415, 1996.

Distribution

1 Christopher Weber
University of Wisconsin-Madison
1500 Engineering Drive
Madison, WI 53706

1 Riccardo Bonazza
University of Wisconsin-Madison
1500 Engineering Drive
Madison, WI 53706

1 0747 Ben Cipiti, 6223
1 0899 Technical Library, 9536 (electronic copy)